

DIRECT MEASURE OF BAND EDGE OPTICAL ABSORPTION OF
SILICON NANOSTRUCTURES USING PHOTOTHERMAL
DEFLECTION SPECTROSCOPY

by
San Theingi

© Copyright by San Theingi, 2015

All Rights Reserved

A thesis submitted to the Faculty and the Board of Trustees of the Colorado School of Mines in partial fulfillment of the requirements for the degree of Master of Science (Materials Science).

Golden, Colorado

Date _____

Signed: _____
San Theingi

Signed: _____
Dr. Reuben T. Collins
Thesis Advisor

Golden, Colorado

Date _____

Signed: _____
Dr. Ryan Richards
Professor and Head
Materials Science Program

ABSTRACT

Quantum confined silicon nanoparticles (Si-NPs) are a promising material for optoelectronic applications. In this thesis, I studied the band edge optical absorption of free standing Si-NPs and Si-NPs in an amorphous silicon matrix, a composite material also known as nano-crystalline silicon (nc-Si:H). In general, it is difficult to directly observe the absorption threshold in these materials because of silicon's low absorption coefficient. For this study, absorption was measured using photothermal deflection spectroscopy (PDS). PDS is a highly sensitive technique which can directly measure the optical absorption of materials through the generated heat.

The first part of the thesis focuses on the structural and optical properties of size varied free standing Si-NPs. Si-NPs were plasma synthesized and the size control was achieved by using a silicon etchant gas. Both photoluminescence (PL) and PDS absorption spectra showed a blue shift with decreasing Si-NP size. An important outcome from this study is that a ~ 300 meV difference between the PL peak and absorption edge was observed which indicates that PL is a defect related process.

The second part of the thesis presents the optical absorption of nc-Si:H as a function of crystal volume fraction (X_c). A low energy enhancement in absorption relative to amorphous silicon by itself is seen in the material with high X_c . In addition, two different bandgaps, one close to amorphous silicon and another close to bulk crystalline silicon, were extracted from this material which indicates that the enhancement in absorption is due to optical transitions directly involving Si-NPs. Based on the energy of the absorption, softening of the quantum confinement when Si-NPs are imbedded in an amorphous silicon matrix is confirmed.

TABLE OF CONTENTS

ABSTRACT	iii
LIST OF FIGURES	vi
ACKNOWLEDGMENTS	viii
CHAPTER 1 GENERAL INTRODUCTION	1
CHAPTER 2 EXPERIMENTAL METHODS	8
2.1 Synthesis of Silicon Nanoparticles, Amorphous Silicon and Nanocrystalline Silicon using Plasma Enhanced Chemical Vapor Deposition	8
2.1.1 Synthesis of Sulfur Hexafluoride Treated Free Standing Silicon Nanoparticle Thin Films using Nanoparticle Reactor	9
2.1.2 Synthesis of Hydrogenated Amorphous Silicon using Dual Zone Reactor	11
2.1.3 Synthesis of Hydrogenated Nanocrystalline Silicon Thin Films using Dual Zone Reactor	12
2.2 Determination of Thickness of the Thin Film	15
2.3 Photothermal Deflection Spectroscopy	16
2.4 Photoluminescence Spectroscopy	20
2.5 Raman Spectroscopy	22
2.6 X-ray Diffraction	24
2.4 Transmission Electron Microscopy	24
CHAPTER 3 INTERPRETATION OF PHOTOTHERMAL DEFLECTION SPECTROSCOPY DATA	25
3.1 Optical Absorption Spectrum of a Disordered Material	25
3.2 Determination of the Bandgap and the Urbach Energy of Amorphous Silicon	27
3.3 Determination of the Bandgap of Si-NPs Taking into Account of Polydispersity in Size	30

3.4	Artificial Enhancement of Surface Absorption in the Sub-gap Absorption Spectra for Samples Less than 1 μm Thick	35
CHAPTER 4	SIZE AND BANDGAP CONTROL OF PLASMA SYNTHESIZED SILICON NANOPARTICLES THROUGH DIRECT INTRODUCTION OF SULFUR HEXAFLUORIDE.....	38
4.1	Acknowledgments	49
CHAPTER 5	OPTICAL ABSORPTION OF NANOCRYSTALLINE SILICON	51
5.1	Synthesis of Co-deposited nc-Si:H	51
5.2	Determining Crystalline Volume Fraction using Raman Spectroscopy	52
5.3	Absorption Spectra of Co-deposited nc-Si:H with Different X_c	53
CHAPTER 6	GENERAL CONCLUSION AND FUTURE WORK	61
	REFERENCES CITED.....	64
	APPENDIX – PERMISSION.....	70

LIST OF FIGURES

Figure 2.1	(a) Schematic illustration of nanoparticle reactor with a nozzle slit (b) Si-NP thin film.	10
Figure 2.2	Schematic of a-Si:H growth using the dual zone reactor.	11
Figure 2.3	Schematic of nc-Si:H growth using the dual zone reactor.	13
Figure 2.4	(a) Ideal co-deposited nc-Si:H film (b) A more realistic co-deposited nc-Si:H film.	15
Figure 2.5	Processing sequence for thickness measurement.	16
Figure 2.6	Schematic figure of experimental setup of PDS.	18
Figure 2.7	Schematic figure of experimental setup of PL.	21
Figure 2.8	An example of Raman data for nc-Si:H and the Gaussian curves used for fitting to calculate X_c [Image courtesy of Tianyuan Guan].	22
Figure 3.1	(a) Optical absorption spectrum and (b) Density of States Vs Energy of a disordered material.	26
Figure 3.2	Optical absorption spectra of amorphous silicon and crystalline silicon.	28
Figure 3.3	(a) The bandgap extraction of a-Si:H using Tauc plot (b) The slope for determining the Urbach energy of a-Si:H.	29
Figure 3.4	(a) Indirect gap plot of c-Si and SiNPs treated with 9 sccm SF_6 (b) PL spectra of SiNPs treated with 9 sccm SF_6	31
Figure 3.5	(a) Variation of $E_{g, avg}$ values with respect to Linear Data Range (b) Normalized A (i.e. A of sample normalized by A of c-Si) vs Linear Data Range for free standing Si-NPs treated with 9 sccm SF_6	34
Figure 3.6	Indirect gap plot of experimental and model absorption data, and linear fit for Si-NPs treated with 9 sccm SF_6	35
Figure 3.7	Absorption spectra of 260 nm and 1700 nm thick a-Si:H (a) before and (b) after thickness normalization. The grey dotted line circle indicates the defect absorption region.	37
Figure 4.1	(a) Raman, (b) powder XRD and (c) PL of samples with SF_6 gas flow rates of 0 sccm, 1 sccm, 2 sccm, and 5 sccm.	43

Figure 4.2	Raman spectra of the samples in the second series with 0 sccm and 5 sccm SF ₆ in the growth precursor gas.	44
Figure 4.3	TEM images of SiNPs prepared with (a) 0 sccm SF ₆ and (b) 9 sccm of SF ₆	45
Figure 4.4	(a) Experimental absorption curve of bulk crystalline silicon. Measured and modeled absorption curves, linear fit, and PL spectra of SiNPs grown with 0 and 9 sccm of SF ₆ . (b) The PL peak position, extrapolated bandgap, and the center of the Gaussian in absorption vs. SF ₆ flow rate.	48
Figure 5.1	(a) Schematic of how X _c varies across the sample (b) Raman spectra for regions with different X _c - 0%, 7.5%, and 14.5% [Raman spectra courtesy of Tianyuan Guan].	53
Figure 5.2	Optical absorption spectra of (a) nc-Si:H with different X _c and (b) conventional nc-Si:H plotted with absorption of a-Si:H and bulk c-Si as a reference [Reprinted with permission from K. G. Kiriluk, J. D. Fields, B. J. Simonds, Y. P. Pai, P. L. Miller, T. Su, B. Yan, J. Yang, S. Guha, a. Madan, S. E. Shaheen, P. C. Taylor, and R. T. Collins, "Highly efficient charge transfer in nanocrystalline Si:H solar cells," <i>Appl. Phys. Lett.</i> , vol. 102, no. 2013, p. 133101, Apr. 2013. Copyright 2013, AIP Publishing LLC].....	54
Figure 5.3	Bandgap extraction from indirect gap plot (a) at high energy regime and (b) at low energy regime.	55
Figure 5.4	Bandgap extraction of the center and transition region from an indirect gap plot using c-Si absorption spectra as a reference.	56
Figure 5.5	PL spectra of free standing Si-NPs [PL spectra courtesy of Grant Klafehn].	57
Figure 5.6	Bandgap as a function of nanocrystal size [Image courtesy of Dr. Mark Lusk with data referenced from Luo <i>et al.</i> [66], Fernandez <i>et al.</i> [62], Wolkin <i>et al.</i> [67]].	58

ACKNOWLEDGEMENTS

I would first like to thank my mom, my dad and my sister for their love, support and encouragement. Without them I would not be where I am today.

I also would like to thank U.S. Department of Energy and the National Science Foundation under Awards No. DE-EE0005326, the Renewable Energy Materials Research Science and Engineering Center (REMRSEC) under DMR-0820518, the Solar Energy Research Institute for India and the U.S. (SERIUS) under the U.S. Department of Energy subcontract DE AC36-08G028308 and Dr. John M. Poate for the Young Investigator Fellowship.

I would like to express my gratitude towards my advisor, Professor Reuben Collins, and Professor Craig Taylor for their guidance, patience, and knowledge during this journey. Thank you so much to Dr. Chito Kendrick, Dr. Mark Lusk, Dr. Paul Stradins and Dr. Lakshmi Krishna for all their support and advice. I also would like to thank my lab teammates, Grant Klafehn, Idemudia John Airuoyo (JJ), Tianyuan Guan and Gang Chen for being great team members.

Thank you very much to Jim Johnson and Rex Rideout for maintaining the equipment, and Phyllis Johnson and Debbie Haywood for their support.

Special thanks for my fellow graduate students and my friends for their friendship and encouragement.

CHAPTER 1

GENERAL INTRODUCTION

Energy is one of the basic necessities for mankind and studies have shown that current primary energy sources, fossil fuels, will not be able to meet the future energy demand [1]. In addition, there are also environmental concerns on the increasing of CO₂ emission due to burning of fossil fuels [2], and thus, there is a need to find an alternative energy supply which is clean and sustainable.

Renewable energies may be a solution to providing sustainable and clean energy for the future and among the different types of renewable energies available, such as solar, wind, geothermal, etc., solar energy is an attractive candidate. The Earth receives 1.4×10^5 TW power from the Sun and about 3.6×10^4 TW is accessible. In 2012, the world total power usage was 17 TW and this value is much less than 3.6×10^4 TW [2]. Thus, solar energy is a promising candidate for a clean energy source if we can harvest much of this usable energy from the Sun.

Solar cells are devices that can convert the solar energy into electricity. There are different types of inorganic and organic materials available for solar cells, however, silicon has a long-standing history and is one of the top choices as an absorber layer for solar cells because it is an earth abundant, low cost and non-toxic material. Two types of commercially available solar cells made from silicon are crystalline silicon (c-Si) and amorphous silicon (a-Si) solar cells. C-Si solar cells are the most widespread commercially available solar cells and, in single crystal and multicrystalline form, they make up about 90% of the market [2]. Currently, c-Si solar cells hold the efficiency of 25.6% [3], however, these single junction c-Si solar cells are approaching the Shockley-Queisser theoretical efficiency limit which is 29% [4]. In addition, the production cost for c-Si is high as it involves an expensive processing technique to make

highly pure c-Si wafers. Thin film solar cells made from a-Si are less expensive to produce than c-Si. A-Si is a non-crystalline allotrope of silicon. In c-Si, each silicon atom is tetrahedrally bonded to four neighboring silicon atoms, and there exists a well-ordered crystal lattice due to long range order of this tetrahedral structure. In a-Si, however, there is no long range ordering of the atoms. The atoms exist as a random network where not all of them are tetrahedrally bonded to its immediate neighbors, and have different coordination [5]. This coordination defect is the primary defect in a-Si where an atom has too few or too many bonds. When there are too few bonds, it creates unsatisfied bonds, also known as dangling bonds. When there are too many bonds, there is a deviation in the Si-Si bond length and bond angles, and thus this introduces strain bonds. These intrinsic bonding disorder and structural defects create localized states and defect states in the band gap. This can cause significant changes in the electronic and transport properties of the material. In addition to the intrinsic defect states, a-Si can also have induced defects created by external excitation such as illumination, current, etc. One of the most well-known effects is the Staebler-Wronski effect where defects are created in the material by light illumination [6]. The exact nature of this effect is still not fully understood, however, a common explanation is that it is a process where upon light absorption, excess carriers are created and some of these carriers recombine non-radiatively. During this recombination process, it releases enough energy to break a weak Si-Si bond, and thereby creating more dangling bonds. This effect poses a limitation for solar cells application since the material will degrade when it is exposed to sunlight and reduce the cell efficiency over time. Hence, there is a need to push for low cost materials to make solar cells with better stability and with efficiencies that can circumvent the limits of single junction cells.

Quantum confined silicon nanoparticles (Si-NPs) have been of great research interest as a material for solar cells due to their unique opto-electronic properties [7]–[10]. Si-NPs are nanocrystals where dimensions of the crystallite are reduced to less than or equal to twice the Bohr's radius of excitons [11]. In this size regime, the material exhibits quantum confinement effect where the bandgap of the material increases as the size of the crystal decreases. Using this energy confinement property, Si-NPs can be engineered to produce different bandgap material which can be stacked to form all silicon multijunction solar cells [7]. Two of the main power loss mechanisms in single junction are that the cell cannot absorb the photon energy if it is less than the bandgap of the material, and part of the absorbed energy is also lost due to thermalization when the cell absorb photons of higher energy than the bandgap. Multijunction solar cells, on the other hand, allow harvesting different wavelengths of the solar spectrum through the use of layers of different bandgap material and this can boost the efficiency of the cell above the Shockley-Queisser limit.

Nc-Si:H is another material of interest for solar cell application [12]. It is a composite film where silicon nanoparticles are embedded in an amorphous silicon matrix. As mentioned earlier, a-Si suffers from light-induced degradation, however, recent research shows that incorporation of nanoparticles in a-Si matrix has led to reduction in optical degradation [13], [14]. The reason behind better stability of the material is because the excess carriers created in amorphous matrix are transferred to Si-NPs and hence, this reduces the probability of non-radiative recombination in the amorphous matrix, which is the primary source for Staebler-Wronski effect. In addition, it is reported that these carriers can be collected before they thermalize[15] and this rapid transfer of carriers can help mitigate the energy loss due to thermalization process. This property can open up the path to realizing hot carrier collection in

solar cells; these solar cells are of particular interest for creating cells with efficiencies that can surpass the Shockley-Queisser limit as the carriers can be extracted before they can relax to the band tail state in a-Si:H matrix[10]. Hence, nc-Si:H is a promising candidate for producing solar cells with better stability and higher efficiencies.

In semiconductors, sub-gap optical absorption measurements are important as in these types of materials, absorption arising from defects and impurities is often observed at energies below the bandgap and thus, these absorption measurements are important for understanding the density and nature of defects at the band edge, and also the optical bandgap (E_g) of the material[16], [17]. In this thesis, the band edge absorption of two forms of materials is discussed. The first form of material studied is Si-NPs, and as presented in the earlier paragraphs, in order to be able to realize multijunction solar cells, it is important to be able to tune the bandgap of the Si-NPs through size control. In this study, the band edge optical absorption of different sized Si-NPs is measured and the bandgap of the material is extracted using both the experimental results and the results from the model. Another section of the thesis discusses the optical absorption of nc-Si:H where quantum confined Si-NPs are embedded into a-Si:H matrix. When two forms of materials are put together, it is important to understand how the composition and the interfaces (i.e. Si-NPs/a-Si interface) of the material have an effect on the opto-electronic properties of the material. In this work, band edge absorption of nc-Si:H as a function of crystal volume fraction is studied.

The standard method for measuring optical absorption is to use the conventional reflection and transmission (R&T) spectroscopy, however, this technique has limitation in sensitivity for measuring small absorption near band edge. In addition, silicon, being an indirect bandgap material, has low absorption coefficient especially at energies near the gap. Hence,

either very thick (many microns) uniform samples are used, or a technique with higher sensitivity is required to measure the band edge absorption of silicon. Photothermal deflection spectroscopy (PDS), in general, can measure absorbance of orders of magnitude smaller than what a conventional R&T spectroscopy can measure. It is a technique that was first developed in 1980 to measure the absorption edge of amorphous silicon [17], [18]. It can directly measure the optical absorption by detecting a subtle change in temperature of the surrounding medium which is induced by absorbed energy of the sample. The change in temperature is measured through the deflection of a probe beam caused by the change in refractive index of the surrounding medium due to temperature gradient. PDS has been extensively used to study the optical absorption of thin film materials and disordered materials. As described above, the electronic structure of disordered materials has band tails states and deep electronic states which require a highly sensitive technique to probe absorption involving these states. Si-NPs and nc-Si:H studied in this thesis are thin film technology materials and can also be considered as disordered materials. In Si-NPs, even though it has a crystalline core, these Si-NPs are often coated with a-Si tissue and there exists surface states which can also give rise to band tail states like those of amorphous silicon. Nc-Si:H is a form of disordered material because it is an inhomogeneous material and surface states also exist at the Si-NP/a-Si:H interfaces. Hence PDS technique is used extensively in this thesis to probe the sub-gap absorption of these materials and is explained in more detail in Chapter 2 and 3.

This thesis is comprised of five chapters in addition to this introduction chapter. Chapter 2 of the thesis presents overview of the experimental setup and techniques used for depositing and characterizing Si-NPs and nc-Si:H. The reactor setup and the growth parameters used to synthesize Si-NPs and nc-Si:H are outlined. The process for determining the thicknesses of the

films are also discussed. In addition, a detail description of the experimental setup for PDS and photoluminescence is given.

Chapter 3 introduces the reader to the important features of a typical optical absorption spectrum of disordered material and the physical interpretation of these features is given. In addition, the process for extracting the bandgap and Urbach energy of the material is given by using the absorption spectrum of a-Si:H as an example. A detailed account on the theoretical model for determining the bandgap of a polydisperse sample is also discussed. Finally, the artificial enhancement of absorption at the low energy of the spectrum is described.

Chapter 4 discusses the study on size control of isolated Si-NPs accomplished by treating them with sulfur hexafluoride (SF_6) gas. The structural and optical properties of Si-NPs were studied. It was found that the size of Si-NPs reduced from $\sim 5\text{nm}$ to less than 3 nm in diameter when they were treated with SF_6 . Both photoluminescence spectra and the absorption spectra shifted to higher energy with decreasing size. The bandgap of the material was extracted using both experimental data and an indirect gap absorption model. An important outcome from this study is that a $\sim 300\text{ meV}$ difference in energy between PL and absorption edge was observed and this indicates that PL emission is a defect related process.

Chapter 5 describes the study of the optical absorption of Si-NPs that were incorporated into an a-Si:H matrix. The optical absorption spectra of nc-Si:H films with varying crystal volume fraction (X_c) was studied. Due to the nature of the reactor setup, the density of Si-NPs incorporated varied across the sample and this is explained in more detail in Chapter 2. Thus, by scanning different regions of the sample the optical absorption spectra of nc-Si:H with different X_c can be obtained. Enhancement in absorption was observed for energies below the bandgap of a-Si:H for regions with higher X_c . In addition, a bandgap close to that of bulk c-Si can be

extracted for these regions. These features were not observed in the region with low density of Si-NPs, and thus, it suggests that they are related to an increase in density of Si-NPs. One possible explanation is that this extra absorption is due to defects or surface states of Si-NPs. Another explanation is that this absorption arises from optical transitions between the Si-NPs and a-Si:H matrix. To better understand this type of transition, a theoretical gap between the highest occupied molecular orbital (HOMO) of Si-NPs to lowest unoccupied molecular orbital (LUMO) of a-Si:H was calculated for our sample using the approach outline by Lusk *et al.*[19]. The result from the calculation was compared with the bandgap obtained from linear extrapolation of the indirect gap plot. The bandgap obtained from both the experimental data and theoretical calculation were in close range but further analysis is required to better understand the nature of this excess absorption. Finally, Chapter 6 gives a general conclusion of this thesis and the suggested future work.

CHAPTER 2

EXPERIMENTAL METHODS

This chapter gives an overview of the experimental setup and techniques that are used to synthesize and characterize the materials discussed in this thesis.

2.1 Synthesis of Silicon Nanoparticles, Amorphous Silicon and Nanocrystalline Silicon using Plasma Enhanced Chemical Vapor Deposition

The central goal of this study was to determine the optimal silicon nanoparticles (Si-NPs) properties and the distribution of Si-NPs in nanocrystalline silicon (nc-Si:H) thin film for device purposes. The properties of Si-NPs were studied by varying of the size and the composition of nc-Si:H was studied by changing the crystal volume fraction (X_c) of the material. Hence, this study involved synthesis of both free standing Si-NPs and Si-NPs in an a-Si:H matrix. Two types of reactors, a nanoparticle reactor and a dual zone reactor, were used to grow different forms of materials studied in this thesis; Si-NPs, hydrogenated amorphous silicon (a-Si:H) and hydrogenated nanocrystalline silicon (nc-Si:H). The nanoparticle reactor can be used to synthesize only Si-NPs. The dual zone reactor integrates a nanoparticle reactor and conventional plasma enhanced chemical vapor deposition (PECVD) growth zone and can be used to deposit a-Si:H, Si-NPs and nc-Si:H. In this project, the nanoparticle reactor was used to grow free standing Si-NP thin films even though the dual zone reactor also had the capability to grow them. This was mainly to allow for sulfur hexafluoride (SF_6) treatment to Si-NPs for size control. SF_6 can result in a by-product that etches the stainless steel in the dual zone reactor. The techniques for growing Si-NPs and nc-Si:H have been extensively studied in the literature [20]–[22] and the detailed growth parameters for synthesizing free standing Si-NPs, a-Si:H and nc-

Si:H are described in the following subsections. Synthesis of the materials was done by Dr. Chito Kendrick, Grant Klafehn, Tianyuan Guan and myself.

2.1.1 Synthesis of Sulfur Hexafluoride Treated Free Standing Silicon Nanoparticle Thin Films using Nanoparticle Reactor

Si-NPs were grown by using plasma enhanced chemical vapor deposition (PECVD) pioneered by Dr. Uwe Korshagen's research group at the University of Minnesota[20]. Schematic figure of the nanoparticle reactor is shown in Figure 2.1(a) and the detail of the setup is described by Kendrick *et al* [21]. A mixture of precursor gases, argon (Ar) and pure silane (SiH_4), was flowed through the quartz tube, which was surrounded by two radio frequency (RF) electrodes. When RF power was supplied to the electrodes, the potential across these electrodes ionized the gas molecules and created plasma, which was confined between the two electrodes inside the quartz tube. The plasma dissociated the precursor gases and Si-NPs started to nucleate and coalesce as they were carried downstream with gas flow. The Si-NPs were then collected on the mesh or on the glass/quartz substrate which was placed at the exit of the quartz tube. Materials collected using this approach were in powder form, however, PDS measurement required Si-NPs to be in a compact film since the sample was dipped in carbon tetrachloride (CCl_4) to increase sensitivity of the measurement. The material may disperse when the sample is submerged in the CCl_4 solution if Si-NPs are not compact. This could affect the intensity of absorption during the measurement and nanoparticles in the solution may also increase noise in the signal. In order to make a densely packed film, a slit nozzle that is $0.2 \times 8 \text{ mm}^2$ was incorporated at the exit of the quartz tube as shown in Figure 2.1 (a). The nozzle created a pressure differential between the growth zone and the collection chamber. This caused the Si-NPs to be accelerated towards the substrate, producing a densely packed film[22], [23]. An example of a Si-NP thin film sample produced is shown in Figure 2.1(b).

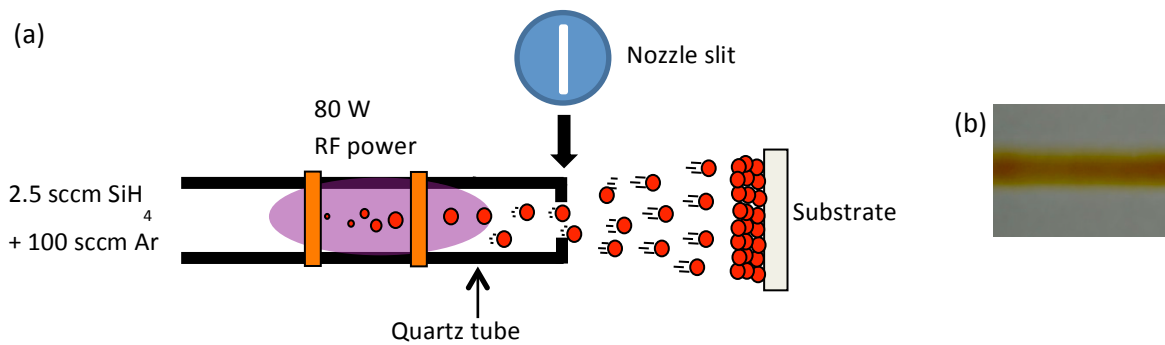


Figure 2.1 (a) Schematic illustration of nanoparticle reactor with a nozzle slit (b) Si-NP thin film

The size of Si-NPs can be controlled by the residence time nanoparticles spend in the plasma, and the residence time is dependent on two main variables, gas flow and reactor pressure[21]. In general, we can reduce the residence time of Si-NPs by increasing the gas flow rate or decreasing the pressure inside the reactor. This will allow us to obtain Si-NPs with smaller diameter. The accessible range of size of Si-NPs using this technique was from 3nm to 8nm. However, previous studies showed that these nanoparticles contained a significant amorphous silicon component which is unfavorable for device purposes[21].

One of the experiments studied in this thesis was using a silicon etchant gas called sulfur hexafluoride (SF_6) gas to control the size of Si-NPs. Dr. Korshagen's research group had previously used SF_6 or carbon tetrafluoride (CF_4) to reduce the size of Si-NPs by using downstream plasma etching: Si-NPs were grown in one region and then were carried downstream with the gas flow to the region with SF_6 plasma for etching[24]–[26]. In our experiment, SF_6 gas was directly introduced into the growth plasma.

In this study, 0 sccm to 9 sccm of SF_6 gas was incorporated into the quartz tube while keeping a constant flow of 100 sccm of Ar and 2.5 sccm of SiH_4 . The reactor pressure was held constant at 8.7 Torr and the RF power was set at 80 W. The effect of adding varying amounts of SF_6 gas into the Si-NPs growth zone was studied.

2.1.2 Synthesis of Hydrogenated Amorphous Silicon using Dual Zone Reactor

a-Si:H was prepared using the dual zone reactor which was comprised of a capacitively coupled plasma (CCP) PECVD reactor and a nanoparticle reactor with separate RF electrodes powered to each reactor. Figure 2.2 shows the schematic figure of the dual zone reactor and the reactor setup is described in more detail by Kendrick *et al*[22]. a-Si:H was grown using only one of the chambers which is the CCP PECVD chamber. This subsection will focus only on the growth of a-Si:H. The synthesis of nc-Si:H using both chambers is discussed in the following subsection 2.1.3.

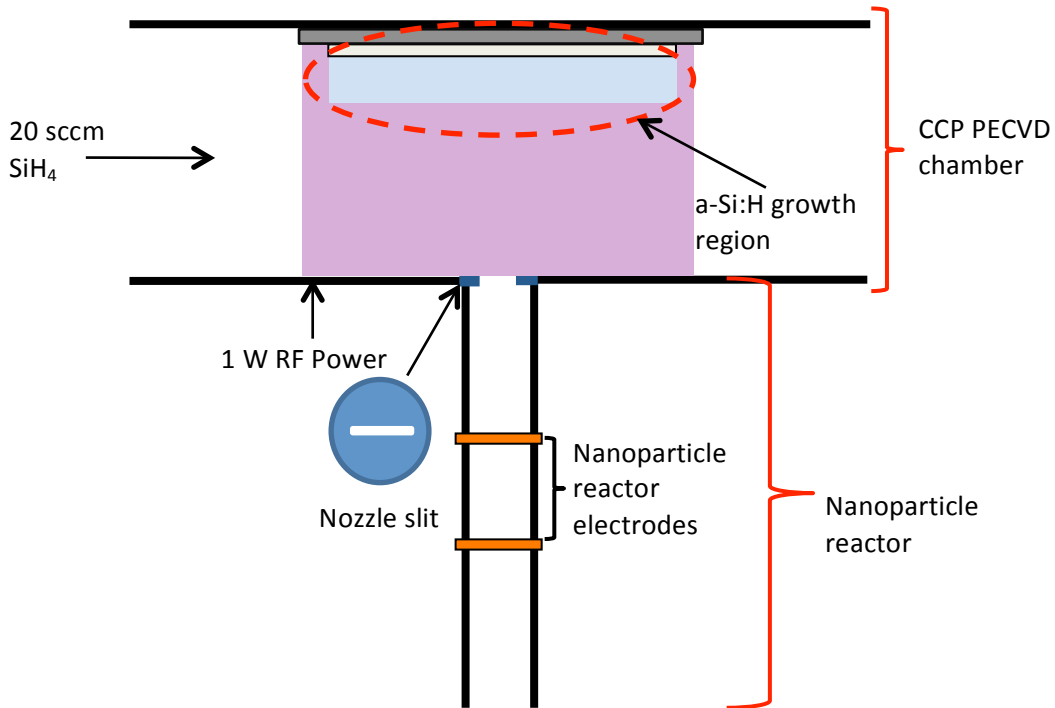


Figure 2.2 Schematic of a-Si:H growth using the dual zone reactor

a-Si:H was deposited by flowing silane gas (SiH_4) into the RF powered plasma inside the CCP PECVD chamber. The plasma excited SiH_4 gas molecules and caused them to dissociate and deposit a-Si:H on the substrate. It is essential to understand the growth rate of a-Si:H as this

will ultimately determine the ratio of Si-NPs to a-Si:H in nc-Si:H films. One of the important parameters for controlling the growth rate of a-Si:H is the power supplied to the electrodes as it controls the dissociation rate of the precursor gas and thus, also the film growth rate [5]. In our study, it was found that increasing power increased the growth rate: while keeping all other parameters constant, changing the RF power from 1W to 1.5W changes the growth rate from 0.13 nm/s to 0.18 nm/s.

Our recipe for depositing a-Si:H was to flow 20 sccm of pure SiH₄ into the reactor, and 1W was supplied to the electrodes. The pressure of the chamber was 500 mT and the temperature of the substrate was held at 200 °C during the growth.

2.1.3 Synthesis of Hydrogenated Nanocrystalline Silicon Thin Films using Dual Zone Reactor

The main goal of this study was to be able to determine the optimal composition of nc-Si:H thin film. An understanding of how nc-Si:H's optical properties change as a function of growth parameters such as those affecting crystal volume fraction (X_c) is essential to this. The result from this study, combined with the knowledge of the Si-NPs properties with varying size as described above, will ultimately allow us to predict the likely optical properties of the material for device purposes.

A typical method for depositing conventional nc-Si:H is to use CCP PECVD and flow hydrogen diluted silane precursor gas into the plasma [27], [28]. This allows for the synthesis of nanocrystals within the a-Si:H matrix, however, the crystallites produced using this technique have dimensions greater than 10 nm and thus, these crystallites are not quantum confined. In order to be able to take advantage of the multi-junction solar cell technology, quantum confined nano-crystallites are required. This section describes a new form of nc-Si:H deposited by using the dual zone reactor described above. As mentioned earlier, the dual zone reactor consisted of

two reactors: a CCP PECVD and a nanoparticle reactor (Figure 2.3). A-Si:H was grown in the CCP PECVD chamber and Si-NPs were synthesized in the nanoparticle reactor and exited into the CCP PECVD growth zone where they were incorporated into the a-Si:H growth to produce nc-Si:H films. A nozzle slit of $0.5 \times 5 \text{ mm}^2$ was included at the exit of the nanoparticle reactor in order to partially isolate the a-Si:H and Si-NPs growth zones, and this allows pressure and gas flow to be controlled independently in each of the reactors. Using this setup, the size of Si-NPs can be controlled by changing the nozzle slit size or changing the flow of the Si-NP precursor gas. Therefore, this allowed quantum confined Si-NPs to be directly injected into the a-Si:H matrix.

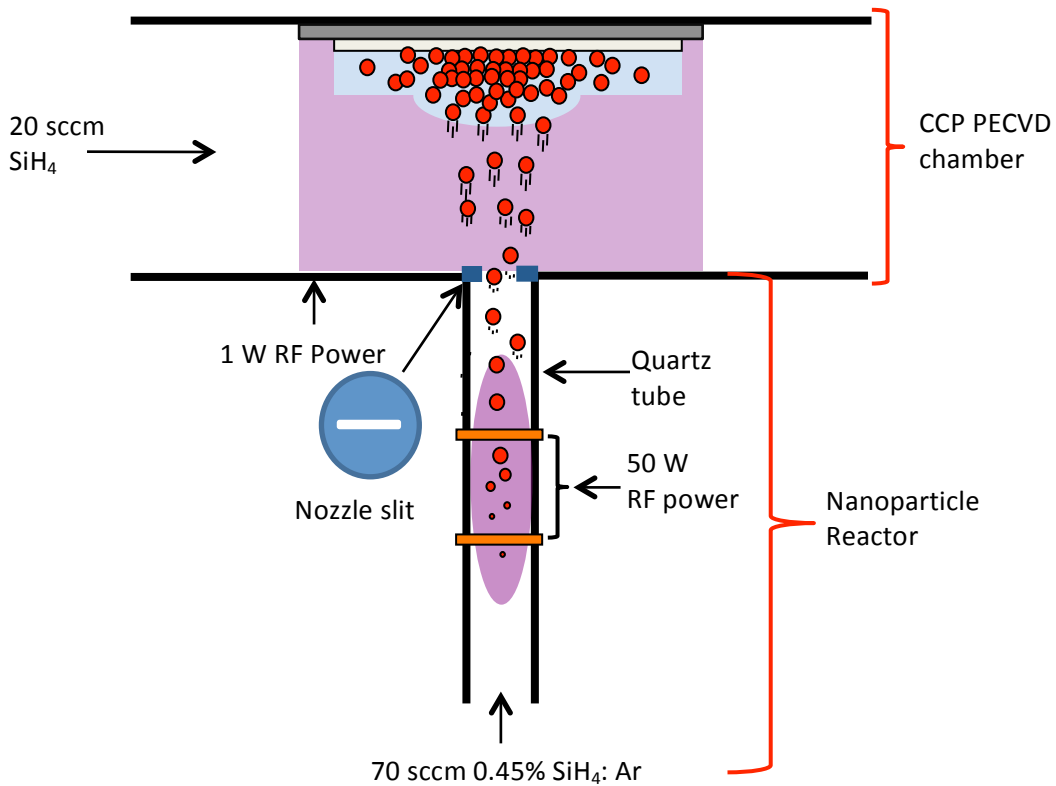


Figure 2.3 Schematic of nc-Si:H growth using the dual zone reactor

In addition to decoupling pressure and gas flow between the chambers, the nozzle in the system also had the effect of producing a densely packed film as described in the earlier section.

In this case, a pressure differential was created between the CCP PECVD chamber and the nanoparticle reactor chamber. A compact film is an important requirement for absorption measurements using PDS when Si-NPs are under study, or when they are incorporated into the a-Si:H matrix for nc-Si:H films.

As mentioned above, the CCP PECVD chamber and the nanoparticle reactor had their own separate electrodes and were partially isolated from each other and thus, the growth of a-Si:H and Si-NPs could be coupled or decoupled. This allowed us to grow pure a-Si:H samples, or free standing Si-NPs films or codeposited nc-Si:H thin films where a-Si:H and Si-NPs were grown simultaneously. In this thesis, Si-NP films were grown in the nanoparticle reactor and a-Si:H and codeposited nc-Si:H films were prepared in the dual zone reactor.

To study how the material's optical properties change with different crystal volume fraction (X_c), varying amounts of Si-NPs were injected into the a-Si:H. Using this reactor, several parameters can be used to control the amount of Si-NPs incorporated into the nc-Si:H film. Some of these parameters include the power and pressure of the CCP PECVD chamber, the power supplied to the Si-NP reactor, gas flow through the Si-NP reactor, and the size of the nozzle slit. In addition, the configuration of the reactor also created variation in X_c across the sample. Schematic figures of an ideal deposition and a realistic deposition of a nc-Si:H thin film are shown in Figure 2.4. In an ideal deposition, a-Si:H and Si-NPs would be uniformly distributed across the sample as shown in Figure 2.4(a). However, due to the reactor configuration, Si-NPs are more concentrated at the center of the substrate, creating higher density of Si-NPs in the middle and lower density of Si-NPs towards the edge as shown in Figure 2.4(b). Hence, X_c was also varied across the sample. Although this structure is not ideal in making an industrial device, it is useful for characterization purposes as it allows for more

freedom in varying X_c of the sample and also, for studying of how the optical properties change with X_c on the same sample. In this thesis, I will focus on how the absorption of nc-Si:H films changes with varying X_c across the sample using the growth conditions described in the following paragraph.

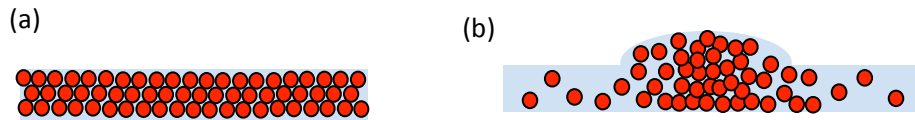


Figure 2.4 (a) Ideal co-deposited nc-Si:H film (b) A more realistic co-deposited nc-Si:H film

For co-deposited nc-Si:H growth, 70 sccm of 0.45% of SiH_4 :Ar was flowed into the Si-NP reactor and 20 sccm of pure SiH_4 was flowed into the CCP PECVD reactor. RF power of 50W was supplied to the nanoparticle reactor electrodes, and 1W was used for the electrodes inside the CCP PECVD chamber. The pressures of 3.7 Torr and 500 mTorr were maintained inside the Si-NP reactor and the CCP PECVD reactor, respectively. The temperature of the substrate was held at 200 °C during the growth.

2.2 Determination of Thickness of the Thin Film

The thicknesses of the films are required to obtain the absorption coefficient of the material. Figure 2.5 shows a schematic figure of the process for obtaining the films' thicknesses. First of all, a majority part of the sample was coated with photoresist to protect the sample. A small region of the sample where the thickness was to be measured was left exposed. Then the sample was put in the reactive ion etching (RIE) chamber and SF_6 plasma was used to etch away the exposed region of the sample. This created a step edge in the film as shown in Figure 2.5. A substrate, such as glass or quartz, which has a much slower etch rate than nc-Si:H was used as an etch top. After etching, the coating of photoresist was removed with acetone and the sample was rinsed with isopropanol. The height of the step edge was then measured using a TENCOR

P-10 surface profilometer to obtain the thickness of the sample which can also be used to determine the growth rate of the sample.

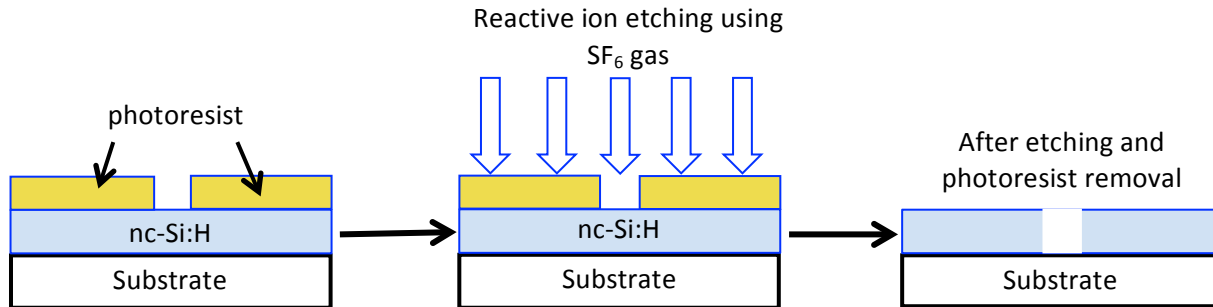


Figure 2.5 Processing sequence for thickness measurement

Using the growth conditions mentioned above, the growth rate of a-Si:H was found to be 0.13 nm/s. The growth rate of nc-Si:H varied across the sample as the sample was not uniform. It was found that at the center of the sample where there is highest density of Si-NPs, the growth rate was 0.28 nm/s and was 0.18 nm/s at the edge where there is the least amount of nanocrystals. Calibrating the growth rate also gives an alternative measure to estimate the crystalline fraction by comparing the a-Si:H growth rate to the edge or center growth rates.

2.3 Photothermal Deflection Spectroscopy

The absorption spectra presented in thesis were obtained using PDS. Figure 2.5 shows a schematic diagram of the experimental PDS setup. The excitation source was the white light beam from a tungsten halogen lamp which was operated at 48 W and was modulated at 7 Hz using a chopper. Typically, the chopper can be operated at frequencies between 7 Hz to 18 Hz. This range of frequency is in the regime where noise from mechanical vibrations are eliminated while also giving enough time for absorbed energy to be completely re-emitted to the surrounding medium[16]. In this study 7 Hz was chosen because it gave the best signal amplitude during optimization of the signal, and this frequency of the chopper was later used as

the lock-in reference. The modulated beam was then passed through a long pass filter to filter out higher order diffraction, and was fed into the monochromator which selected out a particular wavelength (or energy) for which the absorption was to be measured. This modulated monochromatic beam was then focused on the sample where heating occurs from the absorbed energy. The sample was located in a macro fluorescence cuvette (NSG Precision Cells, Inc., Part# M3IR20) that was filled with carbon tetrachloride (CCl_4) solution to increase the sensitivity of the measurement. CCl_4 was chosen because this solvent has a large change in refractive index due to a change in temperature. In addition, it does not absorb light in the energy range of interest for our measurements and does not react with a-Si:H, Si-NPs or nc-Si thin films. One of the assumptions for PDS is that the absorbed energy of the sample at the particular excitation energy is completely re-emitted as heat to the surrounding medium; in this case into the CCl_4 solution. The reemitted heat then created a temperature gradient in the CCl_4 solution near the sample surface which caused changes in refractive index of CCl_4 . This change in refractive index of CCl_4 caused the probe beam, a helium-neon (HeNe) laser (Research Electro-Optics, Model# LAP-036) beam, which was focused parallel to the the sample's surface, to deflect. The amplitude and phase of deflection was then measured by a position sensitive photodiode (United Detector Technology SC-4D) and the output of the detector was fed into the computer-interfaced lock-in amplifier (EG&G PARC model 5208). During the measurement, it is important to monitor the fluctuations in the intensity of the incoming beam as it is not constant over time. In Figure 2.6, a part of the incoming beam was split off by a beam splitter, and was fed into a pyroelectric detector (Molelectron P3) which was used as a reference sensor to measure the intensity of the incoming beam. The output from the detector was fed into another lock-in

amplifier (EG&G PARC models 5207). The PDS signal was then normalized by the intensity of the reference beam and the absorption coefficient, α , was calculated as discussed next.

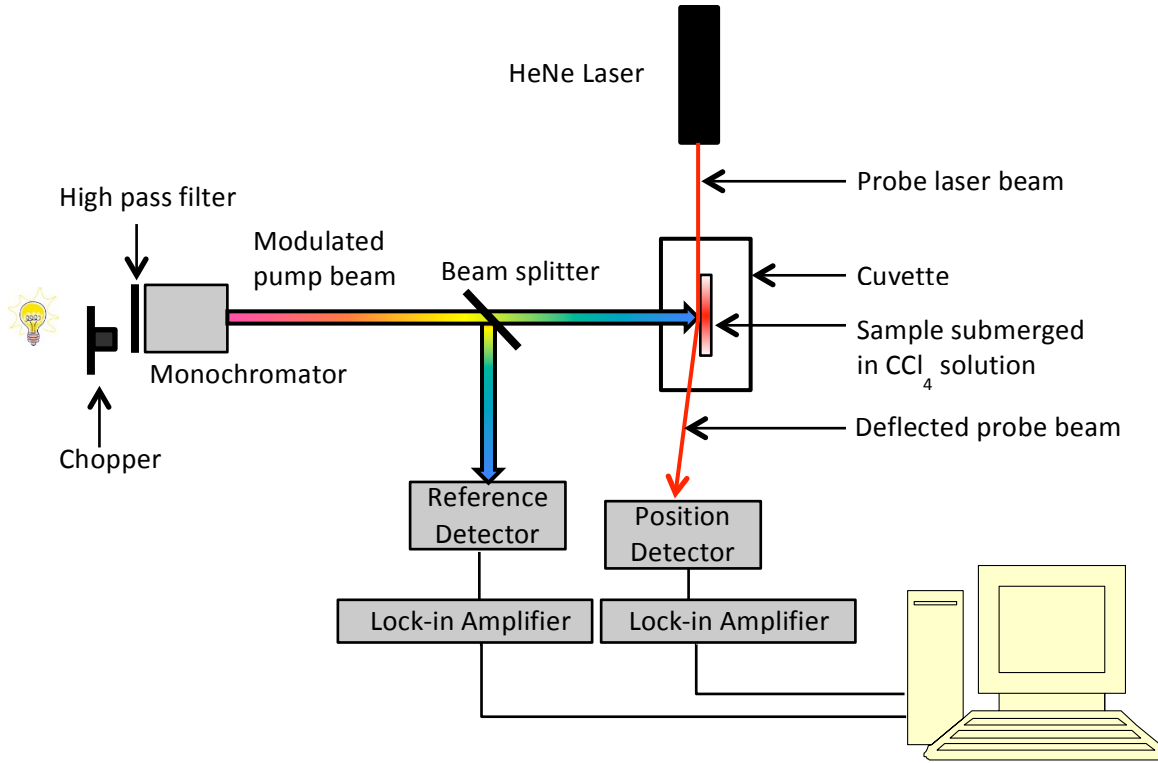


Figure 2.6 Schematic figure of experimental setup of PDS

The deflection signal, S , is given by the following relation [17], [29]:

$$S = T_r \left(\frac{1}{n_0} \right) \left(\frac{dn}{dT} \right) L \left[\frac{dT(z_0)}{dz} \right] e^{i\omega t} + c.c \quad (2.1)$$

where T_r is the detector factor which is a measure of voltage per radian of deflection, $\left(\frac{1}{n_0} \right) \left(\frac{dn}{dT} \right)$ is the relative change of refractive index due to the temperature gradient of the deflecting medium, L is the length of interaction between the heated region and the probe beam, $\frac{dT(z_0)}{dz}$ is the temperature gradient above the sample surface where z_0 is the distance of the probe beam above the sample surface. The exponential term is due to the periodicity of the incoming beam and c.c. is the complex conjugate. If we assume that the film is the only absorbing medium, then

the signal S is dependent only on the term $\frac{dT(z_0)}{dz}$ which is proportional to the film absorption.

Thus, we can generally assume all of the terms except absorption are independent of the excitation wavelength, and the equation for the signal S becomes[16]:

$$S = C A \quad (2.2)$$

where C is a constant comprising of all the constant factors, and A is the film absorption which is dependent on the thickness of the film.

At very high photon energy where the film is completely absorbing, film absorption A is given by $A = 1 - R_F$ where R_F is the reflectance of the front interface. Thus, the signal saturates. For this saturation region S becomes [16]

$$S_{sat} = C (1 - R_F) \quad (2.3)$$

In the region of lower photon energies where the film is not completely absorbing[16],

$$S = C \left[1 - e^{(-\alpha t)} \right] \left[\frac{(1 - R_F)(1 + R_B)}{(1 - R_F R_B)} \right] \quad (2.4)$$

where R_B is the reflectance from the back interface. In order to obtain the absolute value of α , PDS raw data S has to be normalized by S_{sat} using a blackbody reference data. S_{sat} normalization is required to take into account for the material dependent constant factors and a blackbody reference data is needed for the wavelength dependent factors. The blackbody used in the lab was the flat black paint that was sprayed over a quartz substrate. After normalization by S_{sat} and the blackbody reference data, the equation for α as a function of photon energy is

$$\alpha(h\nu) = \left(-\frac{1}{t} \right) \ln \left[1 - \frac{S'(h\nu)}{S'_{sat}} \right] \quad (2.5)$$

where $S'(h\nu)$ and S'_{sat} are the PDS data divided by the blackbody data in the non-saturation and saturation regions, respectively, and α can be calculated if the thickness of the sample is known.

2.4 Photoluminescence Spectroscopy

Optical properties of the materials were also studied using photoluminescence (PL) spectroscopy. In this technique, the electrons are photoexcited across an energy gap, typically the bandgap or mobility gap, and then during the relaxation process, these excited carriers recombine and emit luminescence. PL measures the number of photons as a function of emitted wavelength per certain time interval for a fixed excitation intensity, and this can provide information on the energy levels that are involved in the emission. PL can be used to probe the bandgap of the material, however, care must be taken when deducing the bandgap from the emission spectra as PL cannot detect non-radiative recombination and can be quite sensitive to defect structure. Most materials have some kind of intrinsic defect which is unavoidable, and a defect relaxation process can be radiative, which will give a different emission energy than the bandgap, or non-radiative which can significantly affect decay dynamics and emission efficiency. Thus, the bandgap extracted from this technique may not give the true bandgap of the material and this is observed in the characterization of the SF₆ treated Si-NPs thin films and is discussed in detail in Chapter 4.

Figure 2.7 shows the experimental PL setup used in this study. The light source was a mercury-arc lamp (Newport Apex Arc lamp, Model#66456) with a filter to select the 365nm emission line as the excitation wavelength. The power density was approximately 15 mW/cm². This incoming beam was focused onto the sample using a lens, and the luminescence from the sample was fed into a spectrometer (Princeton Instruments/Roper Scientific, Acton SP300i). A 400 nm long pass filter was used before the spectrometer to avoid focusing scattered excitation light into the system. The spectrometer dispersed the light into different wavelengths using a 150 gr/mm diffraction grating which was blazed at 800 nm. A crystalline silicon charge-coupled device (CCD) array (Princeton Instruments/Roper Scientific, Spec-10:100BR LN) was then used

to detect these photons. The CCD was controlled by using WinSpec software (Version 2.5.23.0). In order to reduce thermal noise, the CCD array was cooled down to -120°C using liquid nitrogen.

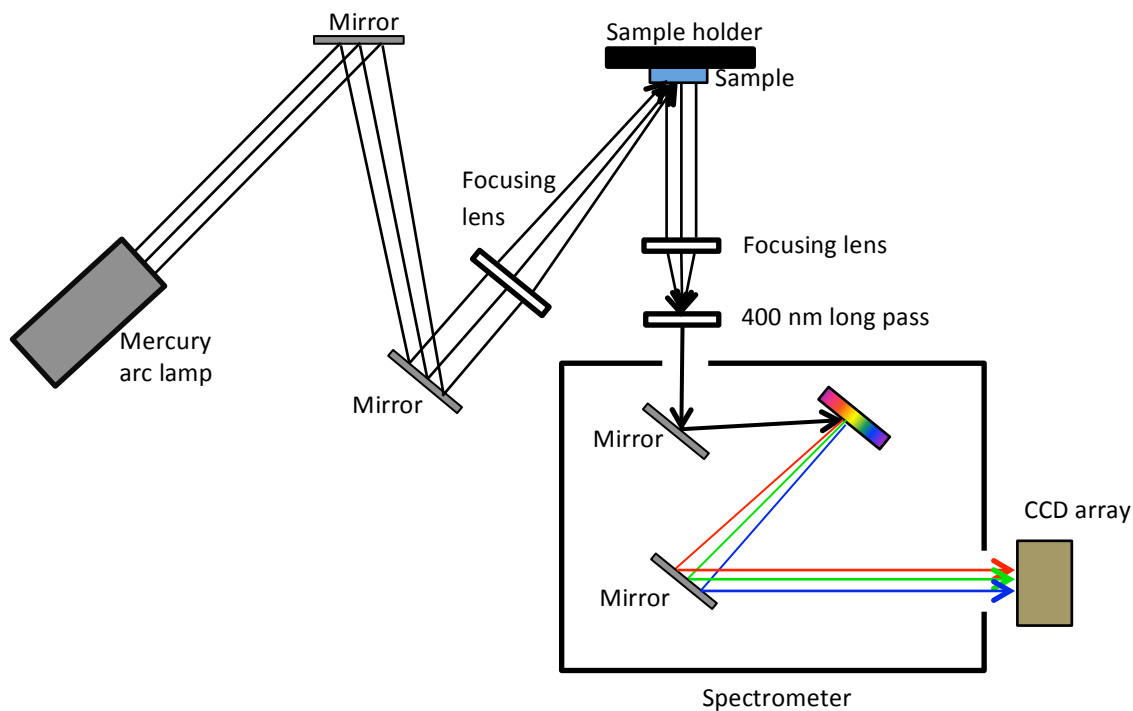


Figure 2.7 Schematic figure of experimental setup of PL

The efficiency of the CCD is not uniform across all the wavelengths. In addition, ambient light leakage into the dark PL room, and weak emission from the glass substrate, sample holder, and other parts of the system can affect the spectra especially if the emission from the sample is very low. Thus, in order to obtain the correct PL spectra of the sample, the background signal and spectral response has to be taken into account. Background signal was corrected by measuring a blank quartz substrate with the same accumulation time as the sample. This background data was then subtracted from the raw data. In order to account for the spectral response, the spectrum from a tungsten lamp was measured. In general this is a blackbody but

over the wavelength range of the measurements it can be considered a fairly flat spectrum. This allowed a correction factor to be determined as a function of wavelength. The spectral correction curve was obtained by Dr. Chito Kendrick and this curve was applied to all the PL spectra included in this thesis. Thus, the final PL data becomes:

$$PL\ Signal_{sample} = (Raw\ Signal - Background\ Signal) * Correction\ factor \quad (2.6)$$

The PL spectra presented here were obtained by Tianyuan Guan, Grant Klafehn and myself.

2.5 Raman Spectroscopy

Raman spectroscopy was used to study the crystallinity of the free standing Si-NPs, and this is discussed in Chapter 4. In addition, Raman was used for nc-Si:H samples to estimate the crystalline volume fraction (X_c) across the sample, and the process for determining X_c is discussed below.

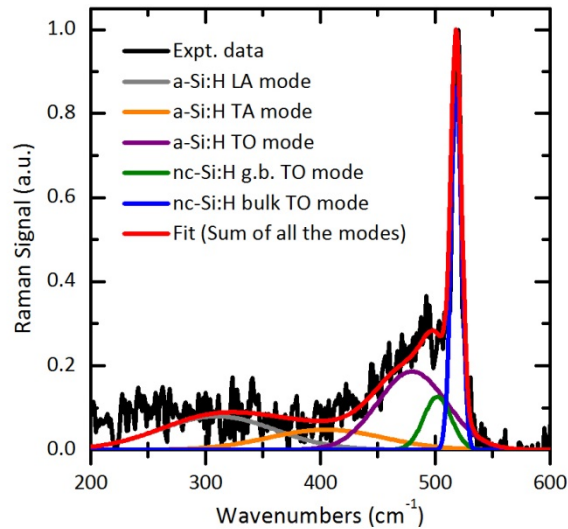


Figure 2.8 An example of Raman data for nc-Si:H and the Gaussian curves used for fitting to calculate X_c [Image courtesy of Tianyuan Guan]

A typical Raman spectrum of nc-Si:H (black curve) is shown in Figure 2.8. The spectrum is comprised of signals relating to different vibrational modes from different phases of the material. There are four vibrational modes for a-Si:H namely transverse optical (TO),

longitudinal optical (LO), longitudinal acoustic (LA) and transverse acoustic (TA) modes. Even though it is uncommon to associate these vibrational modes to an amorphous material, these are the typical terms used when characterizing a-Si:H. Among these four modes, for a-Si:H, the most dominant mode is the TO which is centered at about 480 cm⁻¹ [30], [31]. Bulk crystalline silicon is known to give a peak at about 520 cm⁻¹[30], however, for the crystalline phase of nc-Si:H, the peak often appears at a slightly lower wavenumber than 520 cm⁻¹ because the energy of LO phonon mode for c-Si at the Brillouin zone center red shifted as the size of Si-NPs decreases[32]. Hence a peak around 510 - 520 cm⁻¹ is often attributed to the crystalline phase of the material. In addition to the modes relating to crystalline and amorphous phase of the material, there is another peak at around 498 – 505 cm⁻¹ which represents the phonon mode from the grain boundary of nanocrystals [30]. In order to obtain X_c values, the experimental spectrum was fitted to a series of Gaussian peaks each representing these vibrational modes of a-Si:H, crystalline phase and the grain boundary. An example of the Gaussian fit for a Raman profile is shown in Figure 2.8. The integrated area of three main peaks associated with a-Si:H, crystalline phase and grain boundary was then calculated, and X_c of the sample was computed by using a similar approach as described by Bustarret *et al.* [33]:

$$X_c = \frac{I_{crystalline} + I_{g.b.}}{I_{crystalline} + I_{g.b.} + I_{aSiH-TO}} \quad (2.7)$$

where $I_{crystalline}$, $I_{g.b.}$, and $I_{aSiH-TO}$ are the integrated intensities of the main peaks pertaining to crystalline, grain boundary and amorphous phase of the material. It has been reported that the X_c value obtained using Raman spectra is underestimated [31], and we found this to be the case. However, in this thesis, Raman was used to understand the relative changes in X_c across the sample, and this technique was sufficient to determine the trend. X-Ray Diffraction (XRD) should be used where a more accurate measure of X_c is required.

Raman spectra presented in this thesis were measured by Tianyuan Guan using a WiTec confocal Raman system.

2.6 X-ray Diffraction

X-ray Diffraction (XRD) was another technique that was used to determine the crystallinity of free standing Si-NPs and was measured by Tianyuan Guan using a Siemens Kristalloflex 810 X-ray diffractometer. A more detailed description of the technique and sample preparation for XRD measurements is given in Chapter 4.

2.7 Transmission Electron Microscopy

Transmission electron microscopy (TEM) images were used to determine the size of the Si-NPs and these images were obtained by Dr. Brian Gorman. The details are described in Chapter 4.

CHAPTER 3

INTERPRETATION OF PHOTOTHERMAL DEFLECTION SPECTROSCOPY DATA

The main purpose of this chapter is to introduce a typical absorption spectrum obtained by PDS and to help the reader understand the main features of the absorption spectrum of a disordered material and its physical meaning. In addition, a discussion of additional information that can be extracted using the data from an absorption spectrum and some surface effect artifacts to consider when interpreting the data is given.

3.1 Optical Absorption Spectrum of a Disordered Material

Figure 3.1(a) shows the general features of the optical absorption spectrum of a disordered material. The absorption spectrum is normally broken down into three different regions: the low energy/sub-gap/defect absorption (region A), an exponential absorption edge/Urbach edge (region B), and high energy absorption (region C)[34]. A schematic of the logarithm of the density of states versus energy of a disordered material and the possible optical transitions that correspond to these different regions of the absorption of the spectrum are shown in figure 3.1(b). The optical transitions are represented by arrows. In general, the absorption coefficient $\alpha(E)$ is proportional to convolution of the density of states of both the initial state and the final state, and it is expressed as [35],

$$\alpha(E) = A \int P N_i N_f dE \quad (3.1)$$

where α is the energy dependent absorption coefficient, A is the material dependent constant, E is the photon energy, P is the probability of the transition, and N_i and N_f are the initial and final states of the optical transition.

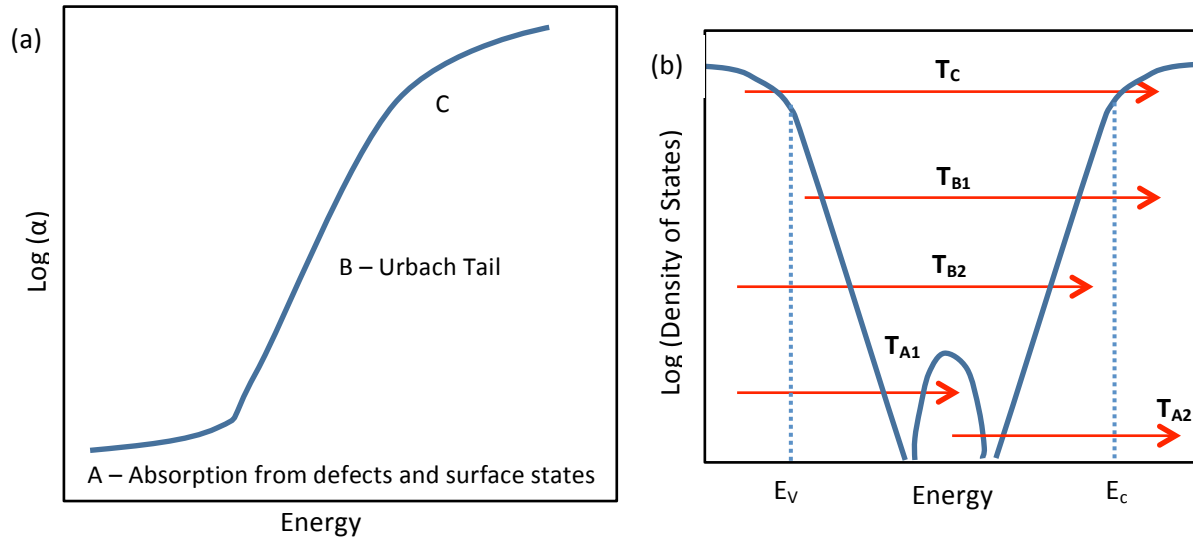


Figure 3.1 (a) Optical absorption spectrum and (b) Density of States Vs Energy of a disordered material

In the low energy regime (i.e. region A), absorption arises from defects and surface states that exist in the material. Thus, the transitions are those involving deep defect states which extend into the forbidden region of the bandgap and the possible transitions are represented by T_{A1} , and T_{A2} in Figure 3.1(b). Comparing the level of absorption in this region can provide qualitative information on the relative defect level between materials, however, care must be taken when interpreting the data in this regime as there can be some surface effect artifacts in the spectra and this is explained in more detail in sub-section 3.4.

Region B of the absorption spectra is commonly known as the Urbach edge and the α value often extends over several orders of magnitude in this region. Absorption in this region is strongly dependent on the material's purity and disorder, and the transitions are from the localized states to the extended states as marked by T_{B1} and T_{B2} in Figure 3.1(b). The absorption spectrum in this region is an exponential rise because as mentioned earlier, absorption is the integral of the product of DOS of N_i and N_f . In this case it is a convolution that involves the

band tail states which vary exponentially in density with energy (See Figure 3.1(b)) and thus the absorption coefficient in the Urbach edge varies with energy in the same exponential manner [36], [37]. The slope of the absorption curve is determined by the width of the band tail states which broadens with increasing disorder. Hence a steeper slope represents better quality material. The absorption edge in this region has the form of [16]:

$$\alpha(h\nu) = \alpha_0 e^{\left(\frac{h\nu}{E_u}\right)} \quad (3.2)$$

where α_0 is a constant, h is Planck's constant, ν is the frequency and E_u is the width of the exponential edge. E_u is also known as the Urbach energy and it can be calculated by taking the reciprocal of the slope of the $\ln(\alpha)$ Vs $h\nu$ curve. Since E_u is related to the slope of the absorption curve which is dependent on the DOS of the band tail state, the quality of the material is often defined by the value of E_u .

The high energy absorption regime (Region C) is normally marked by $\alpha \geq 10^4 \text{ cm}^{-1}$, however this value can vary depending on the material. In this regime, the majority of the absorption comes from the transitions between the extended states of the conduction and valence band and is indicated by T_C in Figure 3.1(b).

3.2 Determination of the Bandgap and the Urbach Energy of Amorphous Silicon

Figure 3.2 shows the experimental absorption spectra of a disordered material and a well-ordered system; amorphous silicon and crystalline silicon. The spectrum for amorphous silicon was experimentally obtained by using the PDS setup in the lab, and the crystalline silicon spectrum is from the data extracted from the literature[38]. It can be seen that for crystalline silicon, the optical absorption edge is marked clearly by the sharp rise in absorption at 1.1 eV, which is the optical gap, E_g , of the material. In amorphous silicon, however, there is no well-defined feature in the spectra to relate to the absorption edge of the material since it is often

camouflaged by the slope of the Urbach tail and low energy defect absorption, which can vary greatly depending on the growth conditions[39]. Hence, a Tauc plot is often used to extract the bandgap of the amorphous semiconductors[40]. In the Tauc approach, assuming the parabolic densities of states for the conduction and valence band, the absorption coefficient of the amorphous semiconductor will vary as $\alpha \propto \frac{1}{hv} (hv - E_g)^2$ for photon energy (hv) greater than the bandgap of the material (E_g), and thus, the bandgap of the material can be extracted by plotting the absorption curve as $\sqrt{\alpha hv}$ Vs. hv and extrapolating the linear region of the curve[40]. The energy at which the extrapolated line intersects with the x-axis gives the bandgap of the material. Figure 3.3(a) shows the Tauc plot for the amorphous silicon spectrum from Figure 3.2, and the bandgap extracted is found to be ~ 1.6 eV which is close to the typical bandgap value for amorphous silicon.

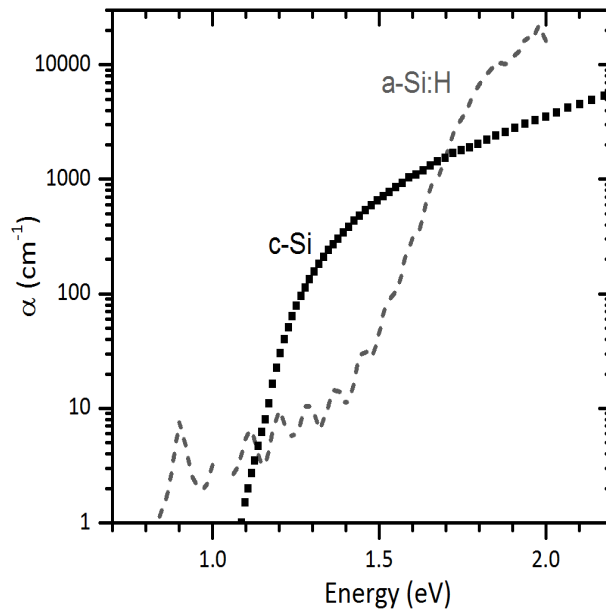


Figure 3.2 Optical absorption spectra of amorphous silicon and crystalline silicon

The Urbach energy (E_u) of the material is determined using the slope of the $\ln(\alpha)$ Vs hv in the energy range from ~ 1.4 eV to ~ 1.8 eV (See Figure 3.3 (b)) and is found to be ~ 60 meV. As

mentioned above, E_u is a measure of the quality of the material and the value for a good amorphous silicon is around 50 meV[5]. This is a strong indication the quality of our material is comparable to good amorphous silicon since the Urbach energy value obtained is close to the typical value.

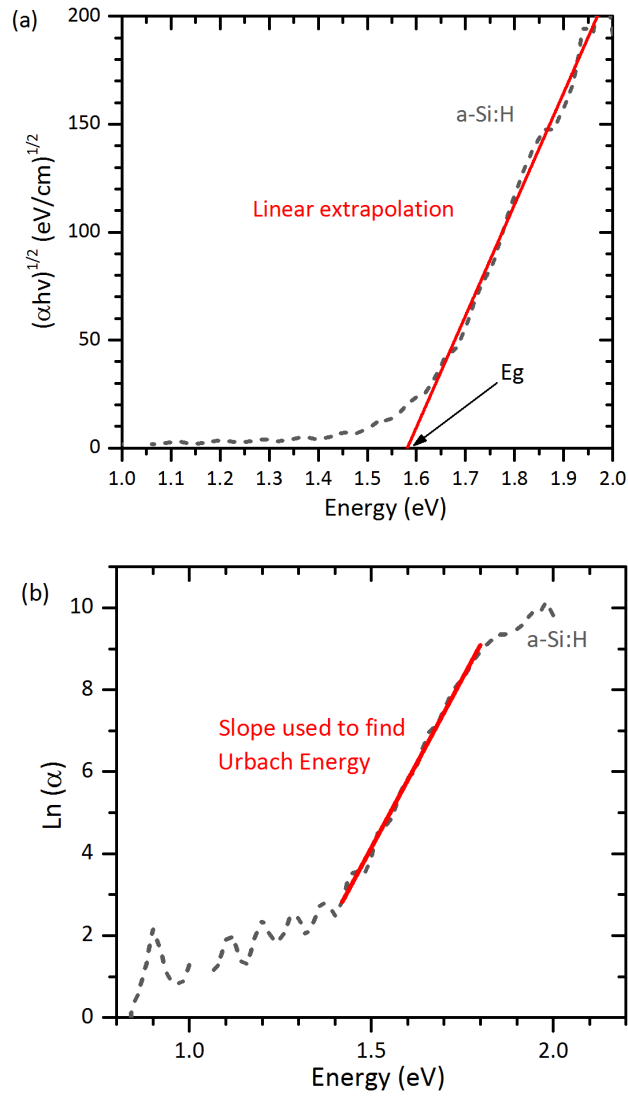


Figure 3.3 (a)The bandgap extraction of a-Si:H using Tauc plot (b) The slope for determining the Urbach energy of a-Si:H

3.3 Determination of the Bandgap of Si-NPs Taking into Account of Polydispersity in Size

In a typical homogeneous semiconductor which is not disordered, depending on the material under study, the bandgap can be estimated by using either the indirect gap or the direct gap plot. Theoretically, for a direct bandgap semiconductor with parabolic band edges, the functional form of the absorption coefficient (α) is $\alpha(h\nu) = \frac{A}{h\nu} (h\nu - E_g)^{1/2}$. Hence a plot of $(\alpha h\nu)^2$ Vs. $h\nu$ gives a straight line and the intercept identifies the bandgap. For an indirect

semiconductor, the functional form becomes $\alpha(h\nu) = \frac{A}{h\nu} \left[\frac{(h\nu - E_g + E_p)^2}{e^{\frac{E_p}{kT}} - 1} + \frac{(h\nu - E_g - E_p)^2}{1 - e^{\frac{-E_p}{kT}}} \right]$ [35]. In

this case, the absorption coefficient is often plotted as $\sqrt{\alpha h\nu}$ Vs. $h\nu$. While the origin of the linear behavior is different from that of the disordered materials described above, in practice, a similar linear fit extrapolation approach is used to determine the bandgap of the material.

However, when the sample is polydisperse, this can affect the extrapolation of the absorption curve for either direct or indirect materials because there is rounding of the absorption curve at the low energies. An example of this is shown in Figure 3.4(a) where absorption of bulk c-Si taken from literature[38] and experimental Si-NPs are plotted as $\sqrt{\alpha h\nu}$ Vs. $h\nu$. The data for experimental Si-NPs is from the sample that has been treated with 9 sccm of SF₆. Bulk c-Si is an indirect semiconductor whereas Si-NPs are an inhomogenous semiconductor because the PL spectrum of the sample has a width to it, which indicates that the sample is polydisperse (Figure 3.4 (b)). A comparison of these two absorption curves shows that while bulk c-Si has a distinct linear regime that extends for about 0.7 eV beyond the bandgap of the material, the spectrum of Si-NPs has curvature at low energy and this makes it hard to determine the correct linear regime. It is important that the linear line is fitted in the correct region so that the bandgap extrapolated is as close to the average bandgap of the material as possible. The wrong choice of the linear range

can result in underestimating or overestimating the bandgap of the material. Hence in this subsection, I will be discussing the modeling of the optical absorption spectra of a polydisperse sample and an approach for determining the linear regime to better estimate the bandgap of the material.

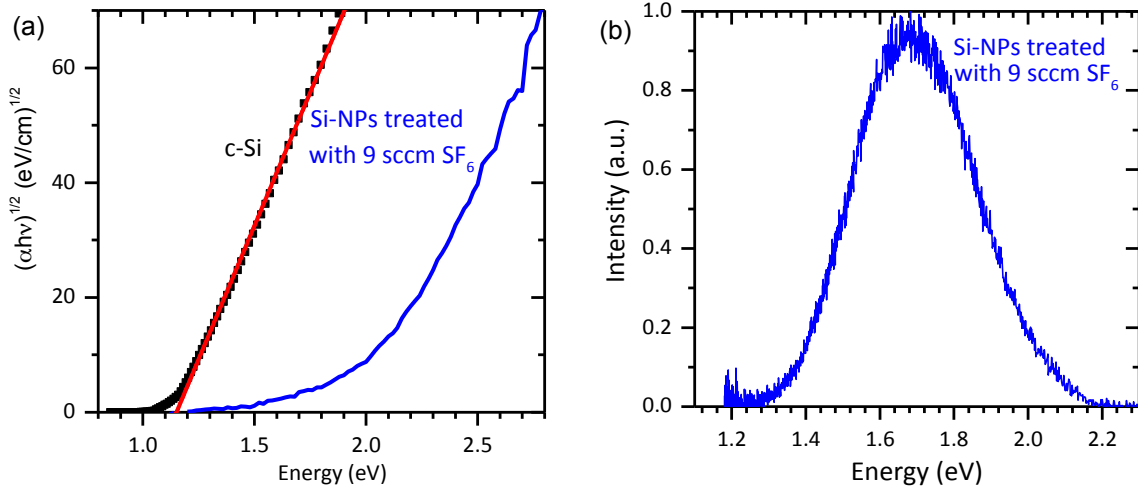


Figure 3.4 (a) Indirect gap plot of c-Si and Si-NPs treated with 9 sccm of SF₆
 (b) PL spectra of Si-NPs treated with 9 sccm of SF₆

The PL spectra of our as grown and SF₆ treated free standing Si-NPs to be discussed in Chapter 4 below show that our sample is polydispersed and thus, in this case, we have modeled the optical absorption to better estimate the band gap of the material by taking into account the size variation in the sample. One of the fundamental questions in modeling the absorption coefficient of quantum confined Si-NPs is whether to model them as direct or indirect semiconductors. Silicon is indirect, but quantum confinement is expected to break k-selection rules and allow direct transitions [41]. For our sample, we fitted the experimental data using both direct and indirect absorption coefficient functions and found that indirect gap model provided a slightly better fit. Thus, in the following, I will present the absorption model for Si-NPs using the indirect gap form.

The optical absorption coefficient, α , of the indirect gap material is given by [35]

$$\alpha(h\nu) = \frac{A}{h\nu} \left[\frac{(h\nu - E_g + E_p)^2}{e^{\left(\frac{E_p}{kT}\right)} - 1} + \frac{(h\nu - E_g - E_p)^2}{1 - e^{\left(\frac{-E_p}{kT}\right)}} \right] \quad (3.3)$$

where A is the material dependent prefactor, E_g is the bandgap, h is the Planck's constant, ν is the frequency of the radiation, k is Boltzmann's constant, T is temperature and E_p is the phonon energy of silicon. To account for the inhomogeneous broadening effects due to size distribution, the absorption coefficient is convoluted with a Gaussian size distribution function

$$G = \frac{1}{\sigma \sqrt{2\pi}} e^{-\frac{(h\nu - E_{g_avg})^2}{2\sigma^2}} \quad (3.4)$$

where σ is the standard deviation and E_{g_avg} is the average bandgap which is the center of the Gaussian in absorption. Thus, in the presence of broadening the absorption becomes

$$\alpha(h\nu) = \frac{A}{h\nu \sigma \sqrt{2\pi}} \int_{-\infty}^{\infty} \left[\frac{(h\nu - E_g + E_p)^2}{e^{\left(\frac{E_p}{kT}\right)} - 1} + \frac{(h\nu - E_g - E_p)^2}{1 - e^{\left(\frac{-E_p}{kT}\right)}} \right] e^{-\frac{(h\nu - E_{g_avg})^2}{2\sigma^2}} dE_g \quad (3.5)$$

This expression was used in Chapter 4 below to fit the absorption curve for distributions of Si-NPs. For bulk silicon, among the several k-conserving phonon energies, the 56 meV phonon energy is typically used and thus, it was chosen for our calculation. The σ value is the standard deviation obtained from fitting a Gaussian to the PL spectrum and the value ranges from 0.14 to 0.17. The temperature T is the room temperature, which is 300 K. The optical absorption coefficient equation was then fitted to the experimental absorption data using two variables, E_{g_avg} and A .

Since there are two parameters that can be varied for the fit, a number of different combinations of these parameters are possible and this can lead to numerous E_{g_avg} and A values for our material. To find reasonable E_{g_avg} and A values, I used the following approach. First, a different range of experimental data was fitted using the analytical equation above and the

resulting E_{g_avg} and A values were recorded. To give an example of this process, first a specific range of experimental data was chosen to fit using the analytical equation, say from 0.8 eV to 2.7 eV, and the E_{g_avg} and A values for that range was determined. Then another data range, say 0.8 eV to 2.6 eV, was chosen and new E_{g_avg} and A values for the new range were calculated. During this process, a linear data range value was also defined. A linear data range is the range between the E_{g_avg} and the endpoint of the experimental data range. For example, suppose we were fitting the experimental data from 0.8 eV to 2.7 eV, and if the E_{g_avg} value obtained was 2.0 eV, our linear data range would be the end point minus E_{g_avg} , which would be $2.7 \text{ eV} - 2.0 \text{ eV} = 0.7 \text{ eV}$. This range was later used to fit a linear line in the indirect gap plot to extract the bandgap. In order to ensure that we were not choosing a very wide linear data range, we used the knowledge of the linear range from the c-Si indirect gap plot. Figure 3.4 (a) shows that the linear range, which can be used to extract the bandgap of c-Si, extends only about 0.7 eV beyond the bandgap (i.e. from 1.2 eV to 1.9 eV) and this is the range where the parabolic band edge assumption is valid. In order to ensure that the same assumption is valid for our sample, the linear data range chosen for our sample was also limited close to that of 0.7 eV range.

In order to ensure that the A values obtained are reasonable, I used the following approach. As I have mentioned above, A is a material dependent prefactor and since the material under study was also silicon, our A value calculated should be close to that of bulk c-Si. Hence each A value obtained for the sample was normalized by that of bulk c-Si to check how much of this value deviated from c-Si with respect to the linear data range chosen. The A value for bulk c-Si was calculated by using the slope of the indirect gap plot of c-Si. This process of fitting and calculating the linear data range value, E_{g_avg} and normalized A value was repeated for multiple data range. E_{g_avg} vs linear data range and normalized A vs linear data range were then plotted

(See Figure 3.5 (a) and (b)). It was found that for our samples, there is a certain linear data range where E_{g_avg} and normalized A values do not vary much and beyond that they change dramatically. An example of this is shown Figure 3.5 (a) and (b) using the analysis from the free standing Si-NPs sample that was treated with 9 sccm of SF_6 . This is one of the samples discussed in Chapter 4. In Figure 3.5 (a), it can be seen that within 0.45 to 0.75 linear data range, E_{g_avg} value varies by only ~ 0.3 eV but it varies dramatically for linear data range outside that limit. A similar trend was also seen in the normalized A value vs linear data range plot. From ~ 0.45 to 0.75 linear data range limit, normalized A value do not vary much and ranges ~ 0.6 to ~ 1 which means the A value of our sample is close to that of c-Si. Hence this shows that E_{g_avg} and A values chosen within this limit is a reasonable value. For this particular sample, using the linear data limit from 0.45 to 0.75, the E_{g_avg} value falls between 1.9 eV to 2.1 eV and this is the error limit of E_{g_avg} for our data.

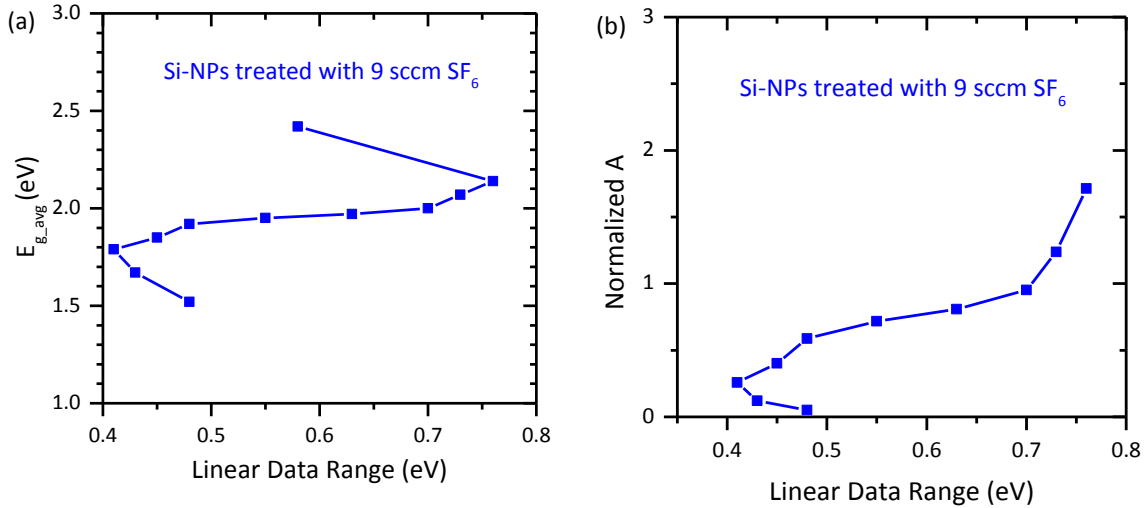


Figure 3.5 (a) Variation of E_{g_avg} values with respect to Linear Data Range (b) Normalized A (i.e. A of sample normalized by A of c-Si) vs Linear Data Range for free standing Si-NPs treated with 9 sccm SF_6

Using this linear data range and E_{g_avg} information, we fitted a linear line to the indirect gap plot of this sample and it is shown in Figure 3.6. The E_{g_avg} value chosen for this plot was 1.95 eV and it was found that the bandgap obtained from the linear extrapolation falls close to this value.

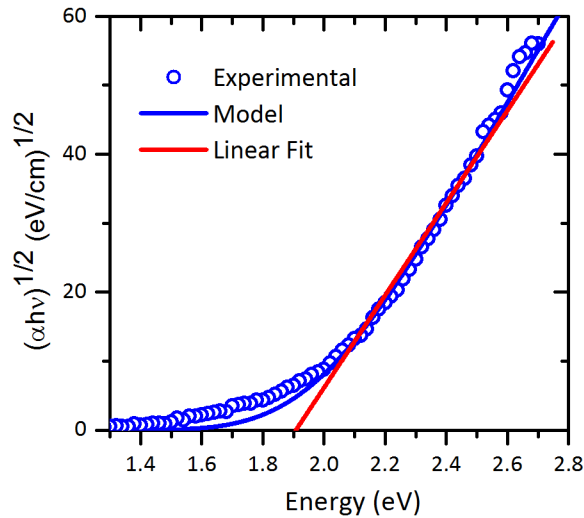


Figure 3.6 Indirect gap plot of experimental and model absorption data, and linear fit for Si-NPs treated with 9 sccm SF₆

3.4 Artificial Enhancement of Surface Absorption in the Sub-gap Absorption Spectra for Samples Less Than 1 μm Thick

One of the characteristics of the absorption spectrum of disordered materials that was discussed above is the sub-gap absorption which is a result of optical transitions involving deep defects that exist in the middle of the gap. Since absorption is proportional to the number of states that are available for the optical transition, a high level of absorption in this regime would imply a high density of the defect states. It would be tempting to use the level of this defect absorption to compare the quality of material between different samples, however, care must be taken when interpreting this low energy absorption as PDS measures absorption from defects

that are related to both the surface and the bulk, and there can be an artificial enhancement of the surface absorption in the spectra when the sample is very thin (i.e. less than 1 μm). As mentioned in Chapter 2, the raw PDS data has to be normalized by the thickness of the material in order to obtain the absorption coefficient, and when there is an absorption contribution from the surface and the bulk and when the total absorption is weak, the signal from PDS (S) can be written as[42],

$$S \propto \alpha_s + \alpha_b t \quad (3.6)$$

where α_s and α_b are the surface and bulk absorption coefficients and t is the thickness of the material. This shows that while the bulk absorption scales linearly with thickness, the surface absorption is constant and thus, the thickness normalization works well only if the defects are related to the bulk and not the surface. Hence, as the sample gets thinner, this normalization process can make the defect absorption of the thin sample to appear virtually higher compared to that obtained from the thick one since the surface to volume ratio increases in the thin sample, making the surface absorption becomes more pronounced in the absorption spectrum. Therefore, in order to obtain the bulk defect density, thick films are required so that the surface absorption does not dominate.

An example of this effect is shown in Figure 3.7(a) and (b) which shows the absorption curves of a-Si:H that have similar defect absorption but are of different thicknesses. The sample for the black curve is ~1700 nm thick and the sample for the red curve is ~260 nm thick. Figure 3.7(a) the total absorption of both of these a-Si:H which have not been normalized by their thickness values and it can be clearly seen that the intensity of defect absorption for these two samples are similar. Figure 3.7(b) shows the PDS data for the same samples but the data have been normalized by the thicknesses. Here the defect absorption for the thin sample now appears

to be much higher than the thick sample. Hence, care must be taken when using this regime to compare the defect absorption of materials. In general, for materials like a-Si and nc-Si:H, at least a 1 μm thick layer of material is required to be able to extract the bulk properties of the material. For this reason, the samples that are used in this thesis for PDS measurement are at least 1 μm thick. The free standing Si-NPs films presented in Chapter 4 are around 5 μm thick and the co-deposited nc-Si:H film discussed in Chapter 5 has the thicknesses that range between ~ 0.9 - 1.5 μm .

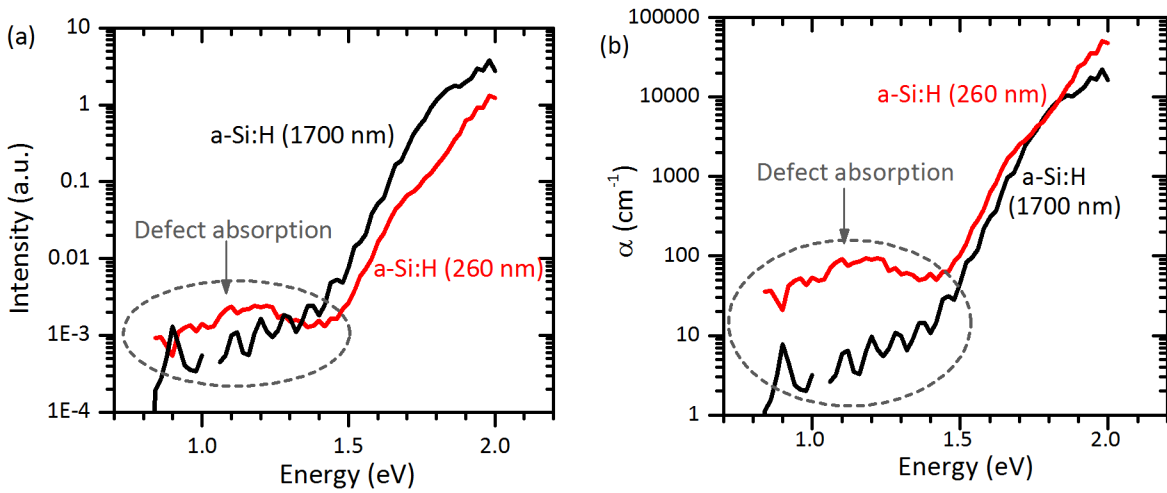


Figure 3.7 Absorption spectra of 260 nm and 1700 nm thick a-Si:H (a) before and (b) after thickness normalization. The grey dotted line circle indicates the defect absorption region.

CHAPTER 4

SIZE AND BANDGAP CONTROL OF PLASMA SYNTHESIZED SILICON NANOPARTICLES THROUGH DIRECT INTRODUCTION OF SULFUR HEXAFLUORIDE

A paper submitted to Applied Physics Letter journal

S. Theingi^{1,2,a, b}, T. Y. Guan^{1,2,a,b}, C. Kendrick^{1,2,4,b}, G. Klafehn^{1,2,b}, B. P. Gorman^{2,b},

P. C. Taylor^{1,2}, M. T. Lusk^{1,2}, P. Stradins^{2,3} and R. T. Collins^{1,2,b,c}

1 - Department of Physics, Colorado School of Mines, Golden, Colorado, 80401, USA

2 - Renewable Energy Materials Research Science & Engineering Center, Colorado School of Mines, Golden, Colorado, 80401, USA

3 - National Renewable Energy Laboratory, Golden, Colorado, 80401, USA

4- Electrical and Computer Engineering, Michigan Technological University, Houghton, Michigan, 49931, USA

Developing silicon nanoparticle (Si-NP) synthesis techniques that allow for straightforward control of nanoparticle size and associated optical properties is critical to potential applications of these materials. In this study, size control is demonstrated through direct introduction of sulfur hexafluoride (SF₆) into the dilute silane precursor of plasma synthesized Si-NPs. Size reduction from 5 to less than 3 nm with increasing SF₆ is demonstrated. The resulting Si-NPs exhibited high crystallinity independent of size. The optical absorption spectra of the Si-NPs in the vicinity of the band gap are measured using photothermal deflection spectroscopy and modeled to extract band gaps. A systematic blue shift in absorption edge due to

^a S. Theingi and T. Y. Guan contributed equally to this work.

^b In this paper, S. Theingi was responsible for measuring, analyzing and modeling of absorption spectra. T.Y. Guan was in charge of Raman and XRD analysis. PL spectra were obtained by both S.Theingi and T.Y.Guan. Synthesis of Si-NPs was done by C.Kendrick and G.Klafehn. TEM images were obtained by B.P.Gorman.

^c Electronic mail: rtcollin@mines.edu.

quantum confinement in the Si-NPs is observed with increasing flow of SF₆. Photoluminescence (PL) spectra show a similar blue shift with size. However, a ~300meV difference in energy between emission and absorption for all sizes suggests that PL emission involves a defect related process. This shows that, while PL may allow size-induced shifts in the band gap of Si-NPs to be monitored, it cannot be relied on to give an accurate value for the band gap as a function of size.

The optical and electronic properties of quantum confined silicon nanoparticles (Si-NPs) have generated considerable scientific and technological interest[7], [8], [43]–[46]. Of particular importance is the ability to use particle size to tune the band gap to values well above that of bulk silicon, thus allowing for emission and absorption of photons in the visible spectrum[8], [43]. In addition, room temperature quantum efficiencies approaching that of direct band gap semiconductors have been observed[9], [47]. Together, these properties would enable tunable, silicon-based, visible wavelength light emitting diodes[45], [46] and biological sensors[44]. Coupled with quantum mechanical phenomena like enhanced multi-exciton generation[48] and hot carrier collection[7], [15], high efficiency photovoltaic cells with tunable band gaps may become possible[7][49].

The quantum confined optoelectronic properties of Si-NPs are directly related to their size[50]. A number of synthesis techniques have demonstrated varying degrees of size control. For example, one approach involves depositing and annealing alternating layers of silicon dioxide (or silicon nitride) and silicon (Si) rich layers of the same insulator. The quantum confined Si-NPs form in the Si rich layers during post deposition annealing with layer thickness controlling Si-NP size[7], [50]. Colloidal synthesis has also proven capable of size control[51]–[53]. Plasma enhanced chemical vapor deposition (PECVD), which is used in this study, allows for nucleation and growth of high quality, quantum confined, crystalline Si-NPs via a dilute

silane plasma[20]. In this approach, the size of the Si-NPs is determined to a large extent by the residence time of Si-NPs in the plasma which is directly related to the gas flow and pressure[21]. Like many techniques for controlling size during growth, however, there is a tradeoff between the accessible size range and crystalline quality; Raman spectroscopy (Raman) and X-ray Diffraction (XRD) spectra reveal an increase in a “hydrogenated amorphous silicon (a-Si:H)-like” component for smaller particles indicating a reduction in crystallinity[21]. An alternative approach to size control during gas phase synthesis involves post-growth etching of Si-NPs grown under conditions leading to high crystallinity. Examples include wet chemical etching[54] and downstream plasma etching using sulfur hexafluoride (SF_6) or carbon tetrafluoride (CF_4), common silicon etchants in plasma processing[24]–[26]. In these studies, the Si-NPs are grown in one reaction zone and then pass through a second zone where plasma etching occurs.

In this study we demonstrate that size control is possible by introducing SF_6 directly into the precursor gas for nanoparticle growth. In addition, we present systematic structural properties as a function of SF_6 flow and demonstrate high crystallinity across a wide size range. One of the complicating issues in correlating changes in the band gap of Si-NPs with growth conditions is the low absorption coefficient of the Si-NPs. Even though breaking of k-selection rules is predicted to enhance absorption relative to bulk silicon[41], it is often difficult to directly detect the absorption threshold, and studies tend to rely on shifts in the energy of the photoluminescence (PL) peak. The PL spectrum, however, can also be influenced by the defect structure of the Si-NPs. In this study we use photothermal deflection spectroscopy (PDS) as a high sensitivity probe of the absorption onset. We compare the PL spectra to this direct measurement of the bandgap as a function of SF_6 flow and observe that both shift systematically

with size. An ~ 320 meV difference in energy between emission and absorption is also observed which suggests PL emission is a defect related process[55].

Si-NPs are plasma synthesized following the approach of Magolini[20] and as described in detail by Kendrick *et al.*,[21] using flows of Ar and pure SiH₄ of 100 and 2.5 sccm, respectively. The SF₆ flow is varied from 0 sccm (no SF₆ gas added) to 9 sccm. A throttle valve in front of the pumping system holds reactor pressure constant at 5.8 Torr as determined by a baraton gauge installed up stream of the quartz tube. The radio frequency (RF) power is set at 80 W. These conditions are selected because they had been demonstrated, in the absence of SF₆, to produce highly crystalline Si-NPs[21]. When the Si-NPs exit the quartz tube, they are collected as a powder on a stainless steel mesh placed in front of the throttle valve. Alternatively, a slit nozzle that is 0.2×8 mm² is placed at the exit of the quartz tube. The nozzle creates a high pressure difference between the growth tube and collection chamber causing the Si-NPs to be accelerated at the substrate to produce a high density specular film[22], [23]. The throttle valve is held wide open with the flow rates creating a reactor pressure of 8.7 Torr. Thin films of Si-NPs are deposited on a quartz slide by passing the slide through the beam of Si-NPs multiple times to build up a coating. The film thicknesses are measured using a TENCOR P-10 surface profilometer and are used later to obtain the true absorption coefficients of the material from PDS measurements. The films used in this experiment are $\sim 5\mu\text{m}$ thick.

Si-NPs are subsequently analyzed using a range of structural, and optical tools, including Raman, XRD, transmission electron microscopy (TEM), PDS and PL. Raman is primarily used to distinguish between amorphous silicon and nano-sized crystalline silicon. Spectra are recorded using a WiTec confocal Raman system with YAG (532 nm) laser excitation in the backscattering configuration. The laser power is held well below the crystallization/sintering threshold during

the measurement. XRD spectra are taken on a Siemens Kristalloflex 810 X-ray diffractometer. PL spectra are collected using an Acton 300i spectrometer with a Princeton Instruments Spec-10:100BR liquid nitrogen cooled silicon CCD detector array. The excitation source is the 365 nm line of a mercury lamp. TEM studies use a Philips CM200 transmission electron microscope operating at 200 keV. Standard FIB (FEI Company Helios 600i, Hillsboro, OR, USA) in-situ liftout specimen preparation techniques are used and final cleaning is completed at 2 kV. Optical absorption spectra are obtained using PDS following the approach of Jackson *et al.*[17]. PDS detects small changes in sample temperature arising from absorption. This is done by detecting the index of refraction gradient in the region just above the sample, which is induced by the heating. The sample is immersed in carbon tetrachloride (CCl_4) solution which has a large thermally induced change in index and increases sensitivity.

To systematically study the effect of including SF_6 on Si-NP structural and optical properties, two sets of samples are prepared. The first series is deposited without a nozzle and collected as powder as described above. This allowed sufficient material to be collected to obtain reasonable signal-to-noise in the XRD measurements. After growth, samples are prepared for XRD by dispersing the Si-NPs in isopropyl alcohol and drop casting onto a Si(100) wafer, forming a layer about 1 mm thick. In addition, some of the powder is compacted between two sapphire wafers for Raman and PL measurements.

In Figure 4.1, we present the Raman (a), XRD (b) and PL (c) spectra from samples prepared with 0, 1, 2, and 5 sccm SF_6 flow during growth. Si-NPs give rise to a sharp TO phonon peak with frequency near the bulk crystalline silicon value of 520 cm^{-1} [56], [57]. They also exhibit a broad shoulder extending to lower energy which is attributed to TO modes of amorphous silicon (a-Si).[58] The relative intensities of the crystalline and amorphous TO modes

have frequently been used to estimate the crystalline fraction of the material[31], [33], [59]. The four Raman spectra in Figure 4.1 have the same shape with a sharp crystalline silicon peak and no obvious change of the crystalline to amorphous peak ratio. This indicates the addition of SF₆ did not significantly change the crystalline quality. In addition, the crystalline Raman peak exhibits a red shift from the bulk crystalline value with increased SF₆ flow. This red-shift has been attributed to confinement of the phonon as Si-NP size decreases[60].

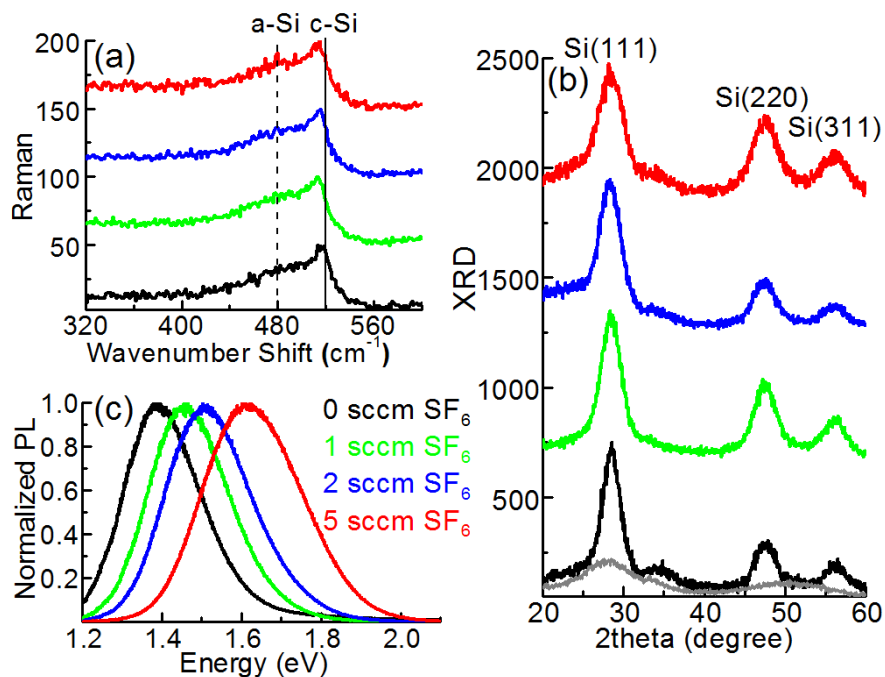


Figure 4.1. (a) Raman, (b) powder XRD and (c) PL of samples with SF₆ gas flow rates of 0 sccm (black), 1 sccm (green), 2 sccm (blue), and 5 sccm (red). In (a), the vertical solid line is the position of the bulk crystalline silicon Raman line and the dashed line is the frequency of the a-Si:H peak. In (b), the grey line is XRD of a-Si:H. The broad peak at ~35 degrees which is most visible in the black curve arises from the Si substrate.

Well defined (111), (220), and (311) crystalline Si diffraction lines are observed at all SF₆ flow rates in the XRD spectra. The lines are broadened compared to bulk crystal silicon, which is consistent with the presence of nanocrystals. Uncertainties in widths are too large, however, to extract Si-NP particle sizes from the broadening. Evidence for the presence of an amorphous

component can be seen in a broadening of the (111) peak to lower angles and some increase in the scattering intensity between the (220) and (311) peaks. It is important to note that the crystal fraction estimated from XRD is much higher than that obtained from Raman. We routinely find, when working with Si-NPs in the quantum confined size range, that Raman overestimates the amorphous component compared to other techniques like XRD and TEM. The central conclusion we draw from Raman, which is in good agreement with XRD, is that crystalline quality does not change with SF₆ flow. The PL plot clearly show that emission blue-shifts with increasing SF₆. The PL shift indicates a decrease in size consistent with the red-shift of the crystalline silicon mode in Raman. As noted above, however, PL is also sensitive to defect structure, hence a direct measurement of the band edge energy as a function of SF₆ is desirable.

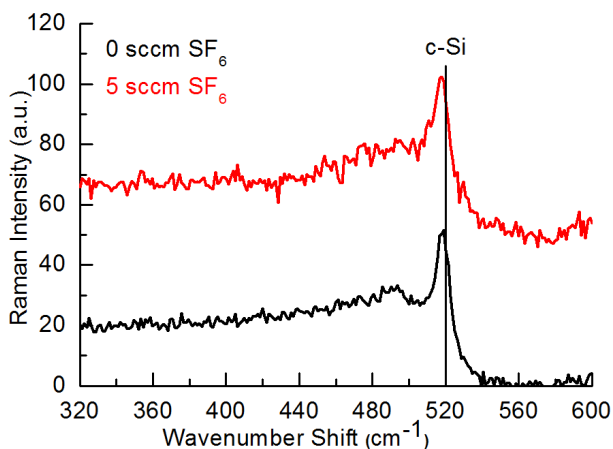


Figure 4.2 Raman spectra of the samples in the second series with 0 sccm (black) and 5 sccm (red) SF₆ in the growth precursor gas. The vertical line indicates the peak position of bulk crystalline silicon.

A second series of samples is prepared for direct PDS measurements of the energy gap. Since the samples are immersed in CCl₄ for the PDS measurements, compact films that do not disperse in the solvent are required. To accomplish this, Si-NP films are deposited on quartz

slides using a nozzle as described above. SF_6 flow rates from 0 to 9 sccm are used. Figure 4.2, shows Raman spectra from samples with 0 sccm and 5 sccm SF_6 flow in the precursor mixture. The inclusion of the nozzle results in higher quality Si-NPs. For example, the ratio of c-Si to a-Si:H Raman peaks is 16% larger than the previous set (see Figure 4.1). Consistent with the first set of samples, the general shape of the Raman spectra, and the ratio of c-Si to a-Si are nearly the same with and without SF_6 .

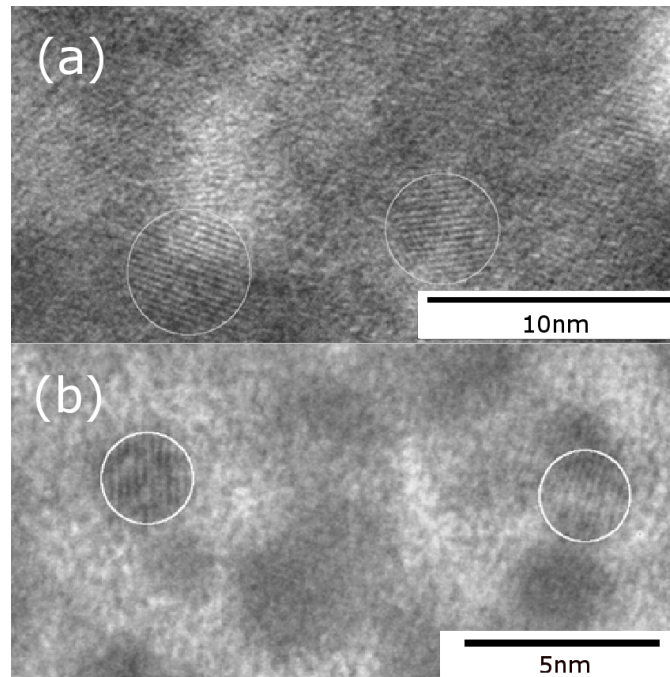


Figure 4.3 TEM images of Si-NPs prepared with (a) 0 sccm SF_6 and (b) 9 sccm of SF_6 . Isolated Si-NPs are highlighted by the white circles.

Figure 4.3(a) and (b) show bright field TEM images for the endpoints of the series, 0 sccm and 9 sccm of SF_6 . Lattice fringes are clear in both, indicating high crystallinity. In addition, the average Si-NP diameter reduces from ~ 5 nm to less than 3 nm with the addition of 9 sccm of SF_6 .

PL and optical absorption spectra near the band edge for the two endpoints (0 and 9 sccm SF₆) are shown in Figure 4.4(a). The absorption is plotted as $(\alpha h\nu)^{1/2}$ vs $h\nu$ where α is the absorption coefficient, h is the Planck's constant, and ν is the frequency of the radiation. For indirect semiconductors, linear extrapolation of this function to the energy axis gives the band gap. A fundamental question of considerable interest is whether to model Si-NPs as direct or indirect semiconductors. Several studies suggest that Si-NPs still exhibit indirect band gap characteristics even in this quantum confined regime [61]–[63]. Studies of porous silicon reported k-conserving phonon features and indirect absorption behavior for light emission at energies comparable to those studied here [41], [64], [65]. Ideally, we would use a functional form tailored to nanoparticles formed of materials with an indirect gap in bulk. The need to consider both electronic and vibrational degrees of freedom, however, complicates the development of such a model and fits are generally made to bulk forms of the absorption. In this study, we used both direct and indirect approaches and found that both approaches lead to similar shifts in band gap with SF₆ flow, however, we present the results with the indirect gap model since it provides a slightly better fit.

A shift in both PL and absorption to higher energies as a function of increased flow of SF₆ is observed and attributed to an increase of the optical gap due to quantum confinement as size of the Si-NPs is decreased. We note that, while as prepared Si-NPs are hydrogen terminated, PDS measurements expose the samples to air resulting in some oxidation. This blue shifts the PL spectrum[24]. For this reason, the PL spectra in Figure 4.4(a) are those recorded once the samples have been exposed to air to allow a direct comparison of PL and absorption. From the PL spectra, it is clear that the Si-NPs are polydisperse. This can affect the extrapolation of the absorption curve to obtain the band gap. To test this, we modeled the optical absorption taking

into account the effect of inhomogeneous broadening by convolving the absorption coefficient with a Gaussian size distribution function. Thus, in the presence of broadening, the optical absorption coefficient equation of the indirect gap material becomes

$$\alpha(h\nu) = \frac{A}{h\nu\sigma\sqrt{2\pi}} \int_{-\infty}^{\infty} \left[\frac{(h\nu-E+E_p)^2}{e^{\left(\frac{E_p}{kT}\right)}-1} + \frac{(h\nu-E-E_p)^2}{1-e^{\left(\frac{-E_p}{kT}\right)}} \right] e^{-\frac{(h\nu-E_{g_avg})^2}{2\sigma^2}} dE \quad (4.1)$$

where α is the absorption coefficient, A is the prefactor which is material dependent, h is the Planck's constant, ν is the frequency of the radiation, k is Boltzmann's constant, T is temperature, E is the bandgap, E_p the phonon energy of silicon, E_{g_avg} is the average bandgap which is the center of a Gaussian distribution in absorption and σ is the standard deviation of the distribution. For bulk silicon, there are several k-conserving phonon energies, but they are usually replaced by the dominant phonon energy of 56 meV and that is used here. σ is estimated by fitting a Gaussian to the corresponding PL spectrum and its value ranges from 0.14 to 0.18 eV. The optical absorption coefficient equation is then fitted to the experimental absorption data (Figure 4.4(a)) using two free parameters, E_{g_avg} , which represents the average bandgap, and A . Fit curves, along with a conventional linear fit and extrapolation of the absorption, are shown in Figure 4.4(a). There are still discrepancies in the absorption at low energies between the experimental and model data which could have arisen from how we chose the band gap broadening function, absorption due to defects, or deviations from the bulk, indirect semiconductor absorption behavior. The band gaps extracted from the linear extrapolation ($E_{extrapolated}$) are systematically lower than the fitted parameter, E_{g_avg} . Since the linear extrapolation neglects the k-conserving phonon energy, the difference is actually ~ 50 meV larger. More importantly, $E_{extrapolated}$ and E_{g_avg} values are higher in energy than the peak of the PL spectrum for all SF₆ flows (figure 4(b)). Comparing the fitted gap to the PL peak shows a systematic difference of $\sim 290 - 340$ meV, which suggests that while the PL emission is definitely

affected by quantum confinement, it likely involves some form of defect related emission.

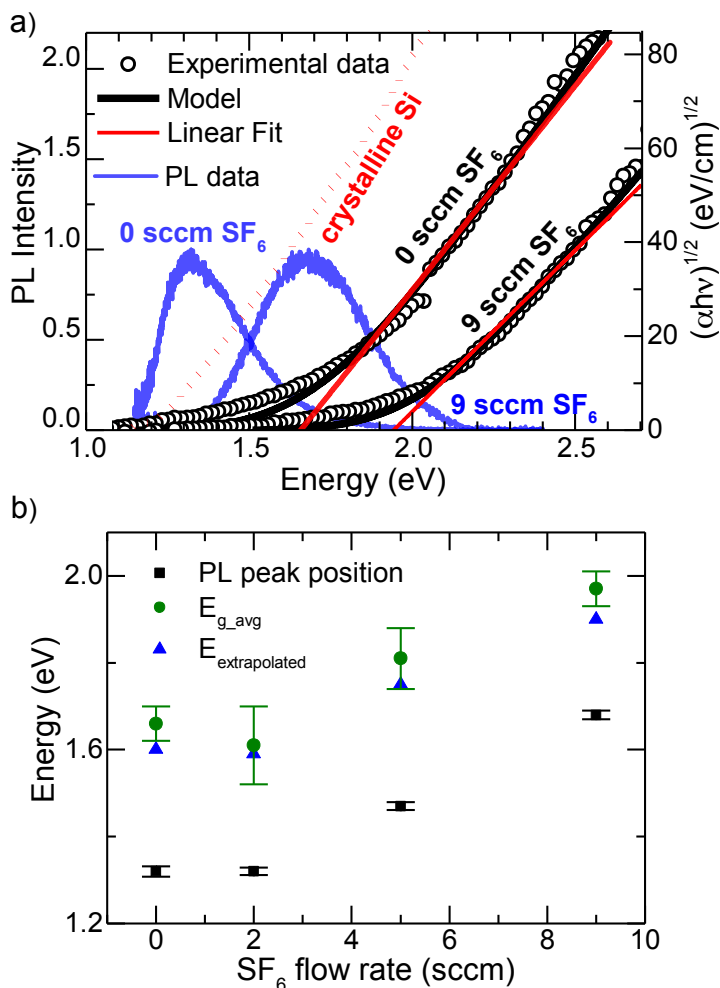


Figure 4.4 (a) Experimental absorption curve of bulk crystalline silicon (red dotted line)[38]. Measured and modeled absorption curves (black circles and solid black curves), linear fit (solid red curves), and PL spectra (blue solid curve) of Si-NPs grown with 0 and 9 sccm of SF₆. The long wavelength asymmetry of the PL spectrum for 0 sccm of SF₆ is caused by the detector response. (b) The PL peak position (black squares), extrapolated bandgap $E_{extrapolated}$ (blue triangles), and the center of the Gaussian in absorption E_{g_avg} (green circles) vs. SF₆ flow rate. The error bar for PL peak position is one standard deviation of the root mean square error between the data and the Gaussian fit. The error bar in E_{g_avg} represents the range of bandgaps that provide a reasonable fit to the experimental data.

Another interesting observation involves the value obtained for the pre-factor, A which varied from 0.8 – 1.2 compared to that obtained by fitting the indirect gap plot of bulk crystalline silicon using published values from Ref. [38]. Since film thickness was used to calibrate the absorption curves, void space in Si-NP films should lead to a reduction in absorption coefficient and hence the pre-factor. While many factors such as composite media effects and changes in selection rules with size can affect A , finding values close to that of bulk silicon suggests a relatively high packing density.

In conclusion we have presented an *in-situ* process for changing the size of plasma-synthesized Si-NPs by introducing SF₆ gas directly into the growth chamber. Size control from 5 to less than 3 nm is demonstrated with the resulting Si-NPs exhibiting high crystallinity independent of size. Using high sensitivity optical absorption measurements, the fundamental absorption edge is directly detected and the expected quantum confinement induced shift of band gap to higher energy with decreasing size is observed. The PL energy, while exhibiting a similar shift, is ~300 meV lower than the absorption edge, indicating defect related emission. This shows that, while PL may allow size-induced shifts in the band gap of Si-NPs to be monitored, it cannot be relied on to give an accurate value for the band gap as a function of size.

4.1 Acknowledgements

This research is based upon work supported by the U.S. Department of Energy and the National Science Foundation under Awards No. DE-EE0005326, DMR-0820518 and is supported in part by the Solar Energy Research Institute for India and the U.S. (SERIUS) funded jointly by the U.S. Department of Energy subcontract DE AC36-08G028308 (Office of Science, Office of Basic Energy Sciences, and Energy Efficiency and Renewable Energy, Solar Energy Technology Program, with support from the Office of International Affairs) and the

Government of India subcontract IUSSTF/JCERDC-SERIIUS/2012 dated 22nd Nov. 2012.

Disclaimer: This report was prepared as an account of work sponsored by an agency of the U.S. government. Neither the U.S. government nor any agency thereof, nor any of their employees, makes any warranty, express or implied, or assumes any legal liability or responsibility for the accuracy, completeness, or usefulness of any information, apparatus, product, or process disclosed, or represents that its use would not infringe privately owned rights. Reference herein to any specific commercial product, process, or service by trade name, trademark, manufacturer, or otherwise does not necessarily constitute or imply its endorsement, recommendation, or favoring by the U.S. government or any agency thereof. The views and opinions of authors expressed herein do not necessarily state or reflect those of the U.S. government or any agency thereof. We also would like to thank Jim Johnson for his support.

CHAPTER 5

OPTICAL ABSORPTION OF NANOCRYSTALLINE SILICON

The previous section discussed the absorption of free standing quantum confined silicon nanoparticles. Chapter 3 summarized the absorption properties of disordered materials and amorphous silicon. In this section, the band edge absorption of quantum confined silicon nanoparticles in an amorphous silicon matrix (i.e. nc-Si:H) is studied. Chapter 2 discussed the growth process for nc-Si:H. In particular it mentioned that when a nozzle is integrated into the Si-NP reactor, the amount of nanoparticles incorporated into the amorphous silicon matrix varies across the sample, and thus, there is a variation in crystalline volume fraction (X_c) across the sample. This allows us to study how the optical properties of the material change with different X_c using a single sample. In this chapter, the absorption of the co-deposited nc-Si:H as a function of X_c is measured using PDS.

5.1 Synthesis of Co-deposited nc-Si:H

The co-deposited nc-Si:H studied in this section was grown using the dual zone reactor discussed in Chapter 2. 110 sccm of 0.45% of SiH_4 :Ar was flowed into the Si-NP reactor and 20 sccm of pure SiH_4 was flowed into the CCP PECVD reactor. The RF power of 80W was supplied to the nanoparticle reactor electrodes and 1.5W was used for the electrode inside the CCP PECVD chamber. The pressures of 3.7 Torr and 500 mT were maintained inside the Si-NP reactor and CCP PECVD reactor respectively. The temperature of the substrate was held at 200 °C during the growth. I mentioned in Chapter 3 that when the sample is thin (i.e. less than 1 μm), surface effects can virtually enhanced the absorption in the low energy region. And thus, a thick sample that is at least 1 μm was grown intentionally for this study.

5.2 Determining Crystalline Volume Fraction using Raman Spectroscopy

In Figure 5.1(a), a schematic diagram of how X_c changes with position across a co-deposited nc-Si:H sample is shown, and Figure 5.1(b) shows the Raman spectra scanned for these regions of the sample. It should be noted here that for the rest of this thesis, the terms center, transition or edge will be used to identify each of the region in the sample. Center refers to the region where we expect highest density of nanocrystals in the material. For this region, X_c value obtained from Raman spectrum for our sample was $\sim 14.5\%$. Transition region is the region where there is medium density of nanocrystals and X_c was found to be 7.5% . Edge of the sample is defined where there is least amount of nanocrystals and X_c estimated from Raman was 0% . In Figure 5.1(b), it can be clearly seen the TO peak associated with crystalline phase becomes more pronounced with increasing X_c . As described in Chapter 2, these X_c values are underestimated and the actual X_c is expected to be much higher. In Chapter 2, I discussed on how X_c can also be estimated from comparison of growth rates between a-Si:H and different regions of the sample. If we would use this approach here to obtain an approximate of X_c for our sample, we found that X_c at the edge was $\sim 20\%$, transition was $\sim 40\%$ and center was $\sim 50\%$. Hence this indicates that, for all the regions of our sample, the density of Si-NPs is much higher than what Raman had predicted. This is an important point to note because from Raman, the edge region has X_c of 0% which would mean that there are no nanocrystals, however, X_c estimated from growth rate was found to be 20% and this indicates that there are nanocrystals in the edge of the sample. Thus, the fact that there is a low density of nanocrystals present in the edge should be taken into account when interpreting the absorption data.

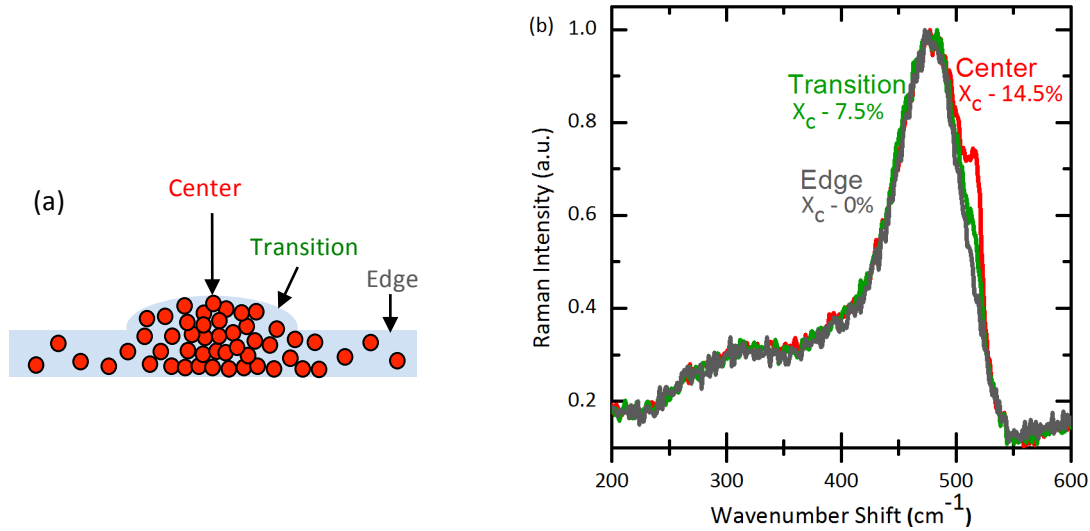


Figure 5.1 (a) Schematic of how X_c varies across the sample (b) Raman spectra for regions with different X_c - 0% (grey), 7.5% (green), and 14.5% (red)
[Raman spectra courtesy of Tianyuan Guan]

5.3 Absorption Spectra of Co-deposited nc-Si:H with Different X_c

Absorption spectra of nc-Si:H with different X_c obtained using PDS are shown in Figure 5.2. The data is plotted with a-Si:H grown without co-deposited Si nanoparticles as discussed in Chapter 3 while the bulk c-Si data is from the literature[38]. For the edge region, the spectral dependence of the absorption is in good agreement with pure a-Si:H. This is to be expected since there is only a low level of Si-NPs present in this region and thus, it does not have a significant impact on the absorption curve. The bandgap of the material extracted using the Tauc plot for this edge region was found to be ~ 1.6 eV (see Figure 5.3 (a)) and the Urbach energy (E_u) obtained from the slope of the $\ln(\alpha)$ vs energy plot was ~ 70 meV. This bandgap is the same as a pure a-Si:H sample calculated in Chapter 3, which was found to be ~ 1.6 eV. The E_u value is a bit higher than the one calculated for a-Si:H which is ~ 60 meV, which could suggest that the a-Si:H has more structural defects when it is grown together with the Si-NPs. It could also be an

indication of a small contribution relating to the surfaces of the Si-NPs. This contribution is discussed next.

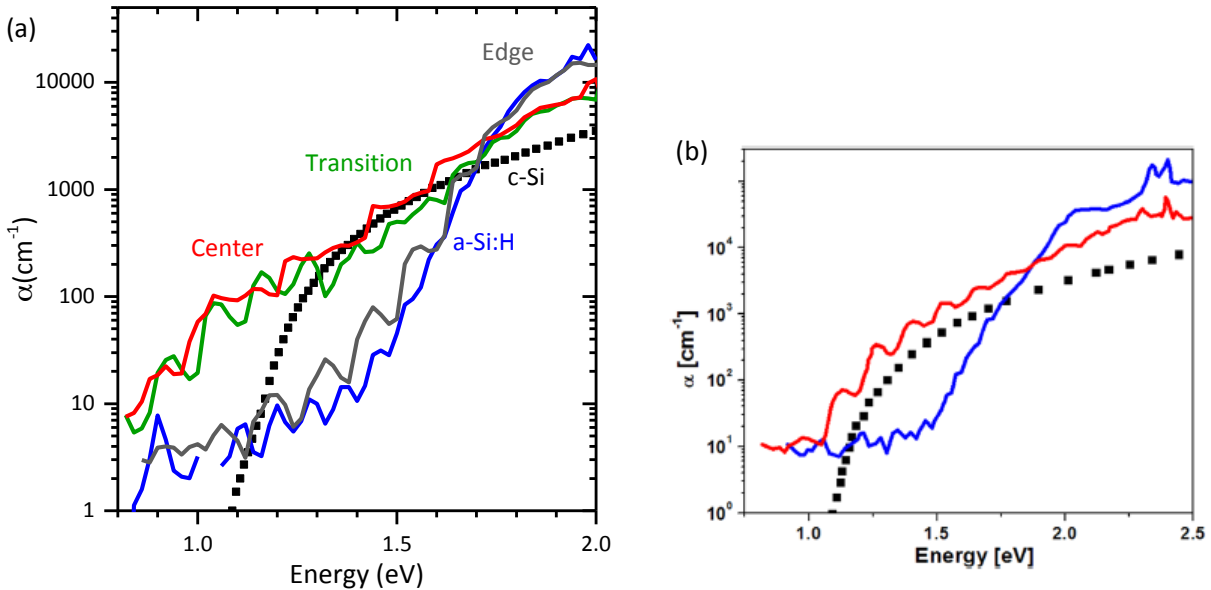


Figure 5.2 Optical absorption spectra of (a) nc-Si:H with different X_c and (b) conventional nc-Si:H (red) plotted with absorption of a-Si:H (blue) and bulk c-Si (black squares) as a reference [Reprinted with permission from K. G. Kiriluk, J. D. Fields, B. J. Simonds, Y. P. Pai, P. L. Miller, T. Su, B. Yan, J. Yang, S. Guha, a. Madan, S. E. Shaheen, P. C. Taylor, and R. T. Collins, “Highly efficient charge transfer in nanocrystalline Si:H solar cells,” *Appl. Phys. Lett.*, vol. 102, no. 1013, p. 103101, Apr. 2013. Copyright 2013, AIP Publishing LLC].

In the center and transition regions, where X_c values are higher, the absorption of nc-Si:H is similar to a typical absorption trend seen in the conventional nc-Si:H as shown in Figure 5.2(b). For the energies above the bandgap of a-Si:H (1.6 eV), absorption of nc-Si:H falls between those of a-Si:H and c-Si. The reduction compared to a-Si:H occurs because the sample is a mixture of about 50% a-Si:H and 50% Si-NPs as indicated by the thickness measurements, and the absorption from the a-Si phase is significantly larger than c-Si in this energy range. The a-Si:H also affects the shape in this region. In the energy regime that is greater than the bandgap of c-Si (1.1 eV) but lower than that of a-Si:H (1.6 eV), the absorption from the center and transition regions varies with energy in a similar fashion to bulk c-Si and is about an order of

magnitude higher than that of the edge. This extra absorption is not observed in the edge region because of the low amount of Si-NPs present in the material. This shows that the excess absorption is due to a significant amount of Si-NPs incorporated in the material and suggests that this excitation of carriers is due to the crystalline phase of the material. This feature is also observed in conventional nc-Si:H as shown in Figure 5.2 (b). Kiriluk *et al.* reported that in conventional nc-Si:H, the extra absorption seen in this energy range is due to the optical transitions in the nanocrystalline phase or in the surface states of the nanocrystals[15].

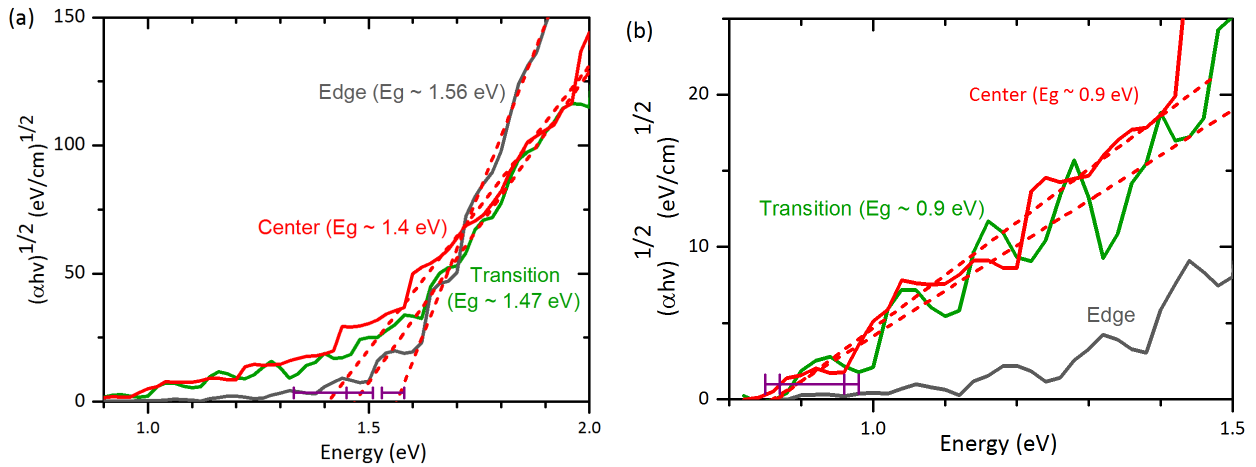


Figure 5.3 Bandgap extraction from indirect gap plot (a) at high energy regime and (b) at low energy regime. The error bar in bandgap is found by fitting the linear regime with different slopes and intercepts and it represents a range of bandgaps that provide a reasonable fit to the experimental data.

In addition, two different bandgaps, ~ 1.5 eV and ~ 0.9 eV, can be extracted using a $(\alpha h\nu)^{1/2}$ vs. $h\nu$ plot which again indicates that there may be absorption from two different phases of the material (See Figure 5.3 (a) and (b)). The first bandgap is lower but is close to that of a-Si:H, which indicates that this absorption is from the a-Si phase. The second bandgap, ~ 0.9 eV, is obtained by fitting the linear regime between 0.8 eV to ~ 1.5 eV as shown in Figure 5.3(b). This 0.9 eV bandgap is an interesting feature because it can be extracted only from the center and transition absorption curves and is not seen in the edge region. This shows that the second

bandgap is related to an increased amount of Si-NPs in the material. It is important to note that although the second bandgap is related to an increase in Si-NPs, and the size of Si-NPs are expected to be in the quantum confined regime, the bandgap is still lower than bulk c-Si.

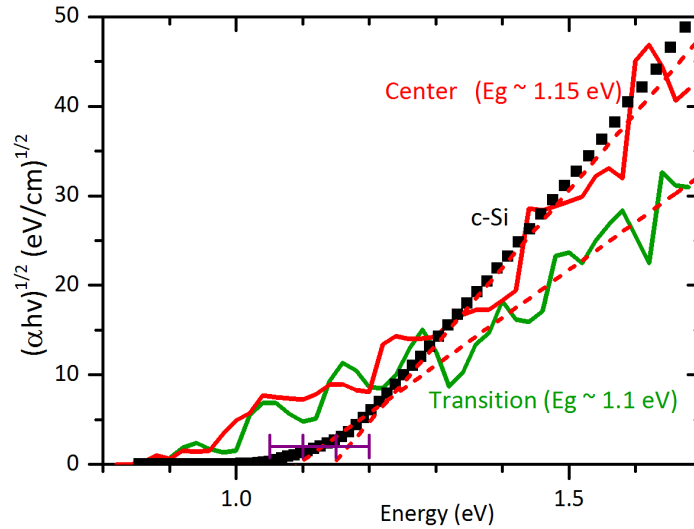


Figure 5.4 Bandgap extraction of the center and transition region from an indirect gap plot using c-Si absorption spectra as a reference. The error bar in bandgap is found by fitting the linear regime with different slopes and intercepts and it represents a range of bandgaps that provide a reasonable fit to the experimental data.

To analyze this further, an indirect gap plot of bulk c-Si is plotted against those from the center and transition region (Figure 5.4). In order to have a more precise comparison between the absorption from nanocrystals and bulk c-Si, the absorption of a-Si:H was first subtracted off from the center and transition spectra before they were plotted as $(\alpha hv)^{1/2}$ vs hv . Here, it was assumed that absorption from amorphous phase in nc-Si:H was comparable to that of pure a-Si:H. Therefore, a pure a-Si:H spectrum was subtracted from the nc-Si:H spectrum to eliminate any amorphous component. Nc-Si:H absorption curves follow a similar trend to bulk c-Si curves for energies above 1.2 eV, but both deviate from c-Si for energies below 1.2 eV. The center has

the same absorption as bulk c-Si and the transition region has a slightly lower absorption. A linear line was fitted between 1.2 eV and 1.7 eV, where the absorption of nc-Si:H from the center overlapped with that of c-Si, and a bandgap of ~ 1.2 eV was extracted for the center region. A similar fit was applied to the absorption spectra of the transition region and a bandgap of ~ 1.1 eV was obtained. Note that both of these bandgaps are close to that of bulk c-Si. One possible explanation is that the incorporated Si-NPs are not quantum confined. However, PL spectra of the free standing Si-NPs deposited using similar growth conditions shows a PL peak at ~ 1.25 eV (Figure 5.5), which indicates that these Si-NPs are quantum confined.

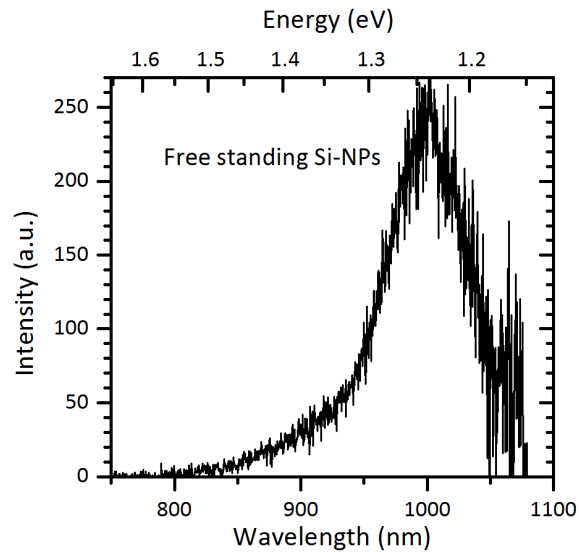


Figure 5.5 PL spectra of free standing Si-NPs [PL spectra courtesy of Grant Klafehn]

Another explanation is that a bandgap close to ~ 1.1 eV is possible if there is optical transition from Si-NPs to a-Si:H matrix. Lusk *et al.* have reported that the nature of quantum confinement changes when nanocrystals are embedded within an amorphous matrix as the matrix modifies the gap between the valence band and the conduction band edges[19]. It is found that the confinement barrier decreases from 1.37 to 0.68 when Si-NPs are placed inside a matrix. This is because for Si-NPs greater than 2 nm in diameter, higher energy valence states appear in the

highest occupied molecular orbital (HOMO) of the nanocrystals which are higher energy than that of the a-Si:H matrix's HOMO. The effective bandgap of the material would then be defined by the gap between the high energy valence states of the HOMO of the nanocrystals and lowest unoccupied molecular orbital (LUMO) of the a-Si:H and thus, the bandgap of the material is lowered. In addition, occupancy of these high energy valence states has nanocrystal size dependence; the larger the nanocrystal, the higher the nanocrystal HOMO orbitals while the LUMO of a-Si:H stays almost constant. Therefore, the effective gap of the material decreases with increasing Si-NPs size.

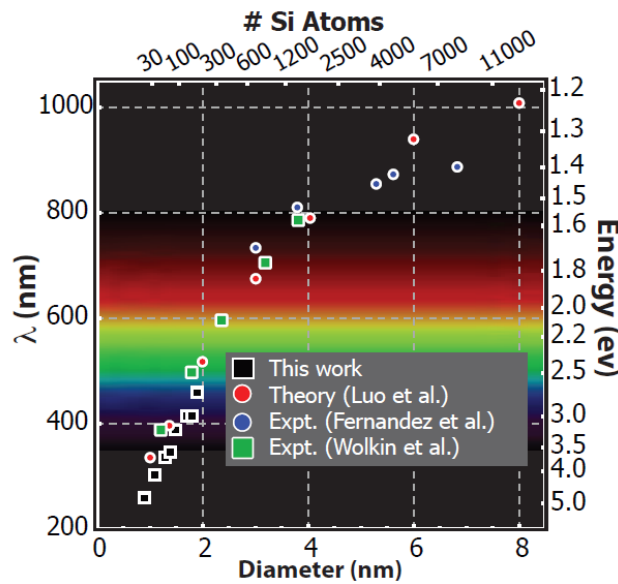


Figure 5.6 Bandgap as a function of nanocrystal size [Image courtesy of Dr. Mark Lusk with data referenced from Luo *et al.*[66], Fernandez *et al.*[62], Wolkin *et al.*[67]]

The effective bandgap of our nc-Si:H can be calculated by using the approach as discussed by Lusk *et al.* [19] if the size of the nanocrystals is known. As mentioned earlier, PL of the free standing Si-NPs shows a peak at ~ 1.25 eV. The study from Chapter 4 shows that there is a difference of ~ 300 meV between the PL peak and the absorption edge for these free standing Si-NPs. Hence, the bandgap for our Si-NPs could range between ~ 1.25 eV to ~ 1.60 eV. Figure

5.6 shows the theoretical bandgap values [66], [67] and experimental PL peak values [62] as a function of Si-NP size. Using this plot, the size of a nanocrystal can be estimated from a given bandgap/PL peak energy. It was found that the size of our nanocrystals range from 4 nm to 8 nm in diameter for the bandgap between ~ 1.25 eV to ~ 1.60 eV. For Si-NPs greater than 2 nm in diameter, the energy levels of the valence band edge (E_{VB}) and conduction band edge (E_{CB}) of the nc-Si:H with respect to the size of the nanocrystals can be found by using the expressions below [19]:

$$E_{VB} = 0.13 - \frac{0.40}{d^{0.68}} \quad (5.1)$$

$$E_{CB} = 0.036 - \frac{0.31}{3.59+d} \quad (5.2)$$

where d is the diameter of the nanocrystal in nm. Note here that the difference between the E_{VB} and E_{CB} will not give the effective bandgap. A correction factor is required to obtain the effective bandgap. This is to ensure that the asymptotic gap value will be equal to that of bulk c-Si. To find this, a constant factor was calculated as d goes to infinity. The second term in the two equations above will become close to zero as d tends to infinity and thus, we will be left with the remaining constants, 0.130 and 0.036. $E_{CB} - E_{VB}$ will then give us a value of -0.094. This value has to be subtracted and the actual bulk c-Si value has to be added to $(E_{CB} - E_{VB})$ expression to ensure that the asymptotic gap value will be equal to that of bulk c-Si. Thus, our final equation becomes

$$E_{effective\ gap} = 0.036 - \frac{0.31}{3.59+d} - \left(0.13 - \frac{0.40}{d^{0.68}}\right) - (-0.094) + 1.12 \quad (5.3)$$

Using this approach the effective bandgap of our nc-Si:H ranges between 1.19 eV to 1.23 eV. For the center region, the bandgap can be fitted within a reasonable range of ~ 1.1 eV to ~ 1.2 eV. The bandgap that can be extracted from indirect gap plot of the transition region ranges from ~ 1.05 eV to ~ 1.15 eV. Thus, it is possible that the bandgap, close to that of bulk c-Si seen in

absorption spectra, could be due to optical transitions from the HOMO of the nanocrystals to the LUMO of the a-Si:H matrix given the error range in fitting the linear region. The error bar in bandgap is found by fitting the linear regime with different slopes and intercepts and it represents a range of bandgaps that provide a reasonable fit to the experimental data. In addition, this optical transition between the Si-NPs and a-Si matrix would indicate that there is coupling between the two phases, an important feature that is necessary for transport in a device.

Another interesting feature of these absorption curves is that the center region has the same absorption as bulk c-Si even though the X_c estimated from the thickness measurement is only 50%. Effective medium effect[68] is a possible explanation for this enhanced absorption, however, our sample consists of only a-Si:H and c-Si and the indices for both are similar. Therefore, there should not be significant effective medium effects. Absorption from defects or absorption between Si-NPs to a-Si:H alone is also hard to justify this enhancement in absorption. A further analysis is required to understand this effect.

One last point to note from Figure 5.5 is the excess absorption seen in both the center and transition spectra for energies below 1.2 eV. As mentioned in Chapter 3, absorption in this regime is due to defects and surface states that exist within the material. Kiriluk et al. inferred that there are surface states related to the Si-NPs[15]. Chapter 4 explains the energy difference between the PL and the absorption edge, which indicates that there are defects related to Si-NPs. Thus, it is possible that the excess absorption seen below 1.2 eV is from defects relating to Si-NPs or Si-NP/a-Si interface and additional study is needed to understand the nature of these defect states.

CHAPTER 6

GENERAL CONCLUSION AND FUTURE WORK

In this thesis, I have presented the optical absorption of non-SF₆ treated and SF₆ treated free standing Si-NPs, and a new form of nc-Si:H where quantum confined Si-NPs are incorporated into the a-Si matrix. The first part of the thesis mainly focuses on studying the structural and optical properties of different sized Si-NPs. Size control of the Si-NPs was achieved by directly incorporating SF₆ into the precursor gas, and it is found that the diameter of Si-NPs reduced by almost a factor of two with increasing flow of SF₆ gas. PL shows a systematic blue shift with size. The absorption edge of these Si-NPs was obtained using PDS, and the bandgap of the material was extracted by modeling the absorption curves using an indirect gap function that was convoluted with a Gaussian broadening. A similar blue shift in the bandgap is observed. In addition, comparing the energy between emission and absorption shows a ~300 meV difference which indicates that PL emission is a defect related process. This defect structure could play a role in excess absorption seen in co-deposited nc-Si:H incorporating Si-NPs produced in this manner.

In the second part of the thesis, absorption spectra of nc-Si:H with different X_c are studied. This was accomplished by examining samples where the growth resulted in a variation in X_c across the sample. It is found that the region near the edge, which has the smallest concentration of Si-NPs, has a spectral dependence of absorption and a bandgap similar to pure a-Si:H but has a slightly higher E_g value, indicating that a-Si grown together with Si-NPs is more defective. For the regions with higher crystallinity, center and transition, the absorption curves of nc-Si:H are similar to that of conventional nc-Si:H. A bandgap of 1.5 eV, which is close to the a-Si:H bandgap of 1.6 eV, is extracted from the higher energy region of the absorption curve.

This is undoubtedly associated with absorption in the amorphous phase of the materials. In addition, there is excess absorption relative to pure a-Si:H at energies below the bandgap of a-Si:H. A second bandgap, near 0.9 eV, can be extracted from this region. This clearly arises from the presence of the crystalline phase. The observation of this excess absorption and its nature is one of the more interesting outcomes of this thesis. A straightforward indirect bandgap fit to the absorption gives a bandgap near 0.9 eV, below that of c-Si. On the other hand, a plot of the c-Si absorption on top of the co-deposited nc-Si:H matches the curve very closely for energies above the Si bandgap but shows excess absorption below the Si bandgap. A bandgap of ~ 1.2 eV can be extracted if a linear line is fitted in the region where nc-Si:H absorption curve overlaps with c-Si. Either view indicated the nc-Si:H has a form of excess absorption near and below the Si bandgap energy. The nature of this absorption is interesting and potentially important. The simplest explanation is that it arises from defects introduced into the system by the inclusion of Si-NPs. As noted above, the shift between the absorption threshold and PL emission energy of free standing nanoparticles suggests the presence of defects. These are presumably at the surface of the Si-NPs. The presence of defects which have been associated with the Si-NP surface has been inferred from the optical properties of conventional nc-Si:H [15]. A more intriguing explanation is that the excess absorption is associated with optical transitions originating in one phase of the material and ending up in the other phase. For example, theoretical studies suggest the valence band (or HOMO) of Si-NPs in an a-Si:H matrix lies in the Si-NP. The LUMO, however, may be located in the a-Si:H at the surface of the Si-NP [19]. This is not what we would call a defect state but rather a localized state created by the effect of the Si-NP on the a-Si:H bonding at the NP surface. Such transitions would also give rise to excess absorption which, depending upon the localization and confinement energy, could

give a bandgap lower than the Si bandgap. A quantitative calculation on the effective bandgap between the HOMO of Si-NPs and LUMO of a-Si:H can be obtained by using the approach described by Lusk *et al.* [19], and it is found that for our material, the effective bandgap ranges between 1.19 eV to 1.23 eV. This range of bandgap is close to the value obtained from one of the linear fits which is ~ 1.2 eV. Given that there is an error bar in these linear fits, a bandgap close to ~ 1.2 eV is possible for our nc-Si:H sample, and thus, it is possible that there are optical transitions between the two phases of the material. Further investigation is required to understand the nature of absorption in this region. Whatever the source, it is clear that co-deposited nc-Si:H can lead to optical absorption very similar to conventional nc-Si:H and with more flexibility to tune Si-NP size.

A suggestion on future work is to perform Constant Photocurrent Method (CPM) [69] measurements to measure absorption that contributes to transport. As mentioned in Chapter 2, PDS detects absorption due to transitions involving all states and thus, absorption measured by PDS also account for the defects states which trap carriers and do not contribute to current. CPM, on the other hand, measures the photocurrent and thus, it measures only the carriers that contribute to the charge transport. Hence, CPM and PDS spectra can be used in combination to separate out the absorption contribution relating transport from the one related to defect states.

It would also be interesting to probe the defect density relating to nc-Si:H. Electron Paramagnetic Resonance (EPR) can be used to determine the defect density and the nature of defects that exists in the nc-Si:H film and scanning different regions of samples with different X_c can provide an insight into understanding the defects in the nc-Si:H in relation to Si-NPs.

REFERENCES CITED

- [1] M. R. Borges Neto, P. C. M. Carvalho, J. O. B. Carioca, and F. J. F. Canafistula, “Biogas/photovoltaic hybrid power system for decentralized energy supply of rural areas,” *Energy Policy*, vol. 38, pp. 4497–4506, 2010.
- [2] M. Hosenuzzaman, N. A. Rahim, J. Selvaraj, and M. Hasanuzzaman, “Global prospects , progress , policies , and environmental impact of solar photovoltaic power generation,” *Renew. Sustain. Energy Rev.*, vol. 41, pp. 284–297, 2015.
- [3] M. A. Green, K. Emery, Y. Hishikawa, W. Warta, and E. D. Dunlop, “Solar cell efficiency tables (version 37),” *Prog. Photovoltaics Res. Appl.*, vol. 19, no. 1, pp. 84–92, 2011.
- [4] W. Shockley and H. J. Queisser, “Detailed balance limit of efficiency of p-n junction solar cells,” *J. Appl. Phys.*, vol. 32, no. 1961, pp. 510–519, 1961.
- [5] R. A. Street, *Hydrogenated Amorphous silicon*. Cambridge University Press, 1991.
- [6] D. L. Staebler and C. R. Wronski, “Optically induced conductivity changes in discharge-produced hydrogenated amorphous silicon,” *J. Appl. Phys.*, vol. 51, no. 1980, pp. 3262–3268, 1980.
- [7] G. Conibeer, M. Green, E. C. Cho, D. König, Y. H. Cho, T. Fangsuwannarak, G. Scardera, E. Pink, Y. Huang, T. Puzzer, S. Huang, D. Song, C. Flynn, S. Park, X. Hao, and D. Mansfield, “Silicon quantum dot nanostructures for tandem photovoltaic cells,” *Thin Solid Films*, vol. 516, pp. 6748–6756, 2008.
- [8] A. G. Cullis & L. T. Canham, “Visible light emission due to quantum size effects in highly porous crystalline silicon,” *Nature*, vol. 353, pp. 335–338, 1991.
- [9] D. Jurbergs, E. Rogojina, L. Mangolini, and U. Kortshagen, “Silicon nanocrystals with ensemble quantum yields exceeding 60%,” *Appl. Phys. Lett.*, vol. 88, no. May 2015, pp. 60–63, 2006.
- [10] M. A. Green, “Third generation photovoltaics: Ultra-high conversion efficiency at low cost,” *Prog. Photovoltaics Res. Appl.*, vol. 9, no. August 2000, pp. 123–135, 2001.
- [11] A. J. Nozik, M. C. Beard, J. M. Luther, M. Law, R. J. Ellingson, and J. C. Johnson, “Semiconductor quantum dots and quantum dot arrays and applications of multiple exciton generation to third-generation photovoltaic solar cells,” *Chem. Rev.*, vol. 110, pp. 6873–6890, 2010.
- [12] S. Guha and J. Yang, “Progress in amorphous and nanocrystalline silicon solar cells,” *J. Non. Cryst. Solids*, vol. 352, pp. 1917–1921, 2006.

- [13] T. Kamei, P. Stradins, and A. Matsuda, "Effects of embedded crystallites in amorphous silicon on light-induced defect creation," *Appl. Phys. Lett.*, vol. 74, no. 1999, p. 1707, 1999.
- [14] G. Yue, B. Yan, G. Ganguly, J. Yang, and S. Guha, "Metastability in hydrogenated nanocrystalline silicon solar cells," *J. Mater. Res.*, vol. 22, pp. 1128–1137, 2007.
- [15] K. G. Kiriluk, J. D. Fields, B. J. Simonds, Y. P. Pai, P. L. Miller, T. Su, B. Yan, J. Yang, S. Guha, A. Madan, S. E. Shaheen, P. C. Taylor, and R. T. Collins, "Highly efficient charge transfer in nanocrystalline Si:H solar cells," *Appl. Phys. Lett.*, vol. 102, no. 2013, p. 133101, Apr. 2013.
- [16] W. B. Amer, Nabil M and Jackson, "Optical properties of defect states in a-Si: H," *Semicond. Semimet. B*, vol. 21, pp. 83–112, 1984.
- [17] W. B. Jackson, N. M. Amer, A. C. Boccara, and D. Fournier, "Photothermal deflection spectroscopy and detection.," *Appl. Opt.*, vol. 20, no. 8, pp. 1333–1344, 1981.
- [18] A. C. Boccara, D. Fournier, W. Jackson, and N. M. Amer, "Sensitive photothermal deflection technique for measuring absorption in optically thin media," *Opt. Lett.*, vol. 5, no. 9, p. 377, Sep. 1980.
- [19] M. T. Lusk, R. T. Collins, Z. Nourbakhsh, and H. Akbarzadeh, "Quantum confinement of nanocrystals within amorphous matrices," *Phys. Rev. B - Condens. Matter Mater. Phys.*, vol. 89, pp. 1–5, 2014.
- [20] L. Mangolini, E. Thimsen, and U. Kortshagen, "High-yield plasma synthesis of luminescent silicon nanocrystals," *Nano Lett.*, vol. 5, no. 4, pp. 655–659, 2005.
- [21] C. Kendrick, G. Klafehn, T. Guan, I. Anderson, H. Shen, J. Redwing, and R. Collins, "Controlled growth of SiNPs by plasma synthesis," *Sol. Energy Mater. Sol. Cells*, vol. 124, pp. 1–9, 2014.
- [22] C. Kendrick, G. Klafehn, T. Guan, S. Theingi, and R. Collins, "Dual reactor deposition of quantum confined nanocrystalline silicon," *2014 IEEE 40th Photovolt. Spec. Conf.*, pp. 2–6, 2014.
- [23] Z. C. Holman and U. R. Kortshagen, "A flexible method for depositing dense nanocrystal thin films: impaction of germanium nanocrystals.," *Nanotechnology*, vol. 21, no. 33, p. 335302, 2010.
- [24] R. W. Liptak, B. Devetter, J. H. Thomas, U. Kortshagen, and S. A Campbell, "SF₆ plasma etching of silicon nanocrystals.," *Nanotechnology*, vol. 20, p. 035603, 2009.

- [25] X. D. Pi, R. W. Liptak, S. A. Campbell, and U. Kortshagen, "In-flight dry etching of plasma-synthesized silicon nanocrystals," *Appl. Phys. Lett.*, vol. 91, no. 2007, pp. 1–4, 2007.
- [26] X. D. Pi, R. W. Liptak, J. Deneen Nowak, N. P. Wells, C. B. Carter, S. A. Campbell, and U. Kortshagen, "Air-stable full-visible-spectrum emission from silicon nanocrystals synthesized by an all-gas-phase plasma approach.," *Nanotechnology*, vol. 19, p. 245603, 2008.
- [27] B. Yan, G. Yue, J. Yang, S. Guha, D. L. Williamson, D. Han, and C. S. Jiang, "Hydrogen dilution profiling for hydrogenated microcrystalline silicon solar cells," *Appl. Phys. Lett.*, vol. 85, no. 2004, pp. 1955–1957, 2004.
- [28] B. Yan, C.-S. Jiang, Y. Yan, L. Sivec, J. Yang, S. Guha, and M. M. Al-Jassim, "Effect of hydrogen dilution profiling on the microscopic structure of amorphous and nanocrystalline silicon mixed-phase solar cells," *Phys. Status Solidi*, vol. 516, no. 3, p. NA–NA, 2010.
- [29] Z. A. Yasa, W. B. Jackson, and N. M. Amer, "Photothermal spectroscopy of scattering media.," *Appl. Opt.*, vol. 21, no. 1, pp. 21–31, 1982.
- [30] C. Droz, E. Vallat-Sauvain, J. Bailat, L. Feitknecht, J. Meier, and A. Shah, "Relationship between Raman crystallinity and open-circuit voltage in microcrystalline silicon solar cells," *Sol. Energy Mater. Sol. Cells*, vol. 81, pp. 61–71, 2004.
- [31] C. Smit, R. A. C. M. M. Van Swaaij, H. Donker, A. M. H. N. Petit, W. M. M. Kessels, and M. C. M. Van de Sanden, "Determining the material structure of microcrystalline silicon from Raman spectra," *J. Appl. Phys.*, vol. 94, no. 2003, pp. 3582–3588, 2003.
- [32] A. K. Arora, M. Rajalakshmi, T. R. Ravindran, and V. Sivasubramanian, "Raman spectroscopy of optical phonon confinement in nanostructured materials," *J. Raman Spectrosc.*, vol. 38, no. August 2015, pp. 604–617, 2007.
- [33] E. Bustarret, M. A. Hachicha, and M. Brunel, "Experimental determination of the nanocrystalline volume fraction in silicon thin films from Raman spectroscopy," *Appl. Phys. Lett.*, vol. 52, pp. 1675–1677, 1988.
- [34] G. D. Cody, "The Optical Absorption Edge of a-Si:H," *Semicond. Semimet. B*, vol. 21, pp. 11–79, 1984.
- [35] J. I. Pankove, *Optical Processes in Semiconductors*. 1971.
- [36] M. V. Kurik, "Urbach rule," *Phys. status solidi*, vol. 8, pp. 9–45, 1971.
- [37] B. I. Halperin and M. Lax, "Impurity-band tails in the high-density limit. I. Minimum counting methods," *Phys. Rev.*, vol. 148, no. 1963, pp. 722–740, 1966.

- [38] M. A. Green, “Self-consistent optical parameters of intrinsic silicon at 300 K including temperature coefficients,” *Sol. Energy Mater. Sol. Cells*, vol. 92, pp. 1305–1310, 2008.
- [39] W. B. Jackson and N. M. Amer, “Direct measurement of gap-state absorption in hydrogenated amorphous silicon by photothermal deflection spectroscopy,” *Phys. Rev. B*, vol. 25, no. 8, pp. 5559–5562, 1982.
- [40] J. Tauc, “Optical properties and electronic structure of amorphous Ge and Si,” *Mater. Res. Bull.*, vol. 3, pp. 37–46, 1968.
- [41] D. Kovalev, H. Heckler, G. Polisski, and F. Koch, “Optical Properties of Si Nanocrystals,” *Phys. Status Solidi*, vol. 215, no. 2, pp. 871–932, Oct. 1999.
- [42] W. B. Jackson, “Optical absorption spectra of surface or interface states in hydrogenated amorphous silicon,” *Appl. Phys. Lett.*, vol. 42, no. 1983, p. 105, 1983.
- [43] W. L. Wilson, P. F. Szajowski, and L. E. Brus, “Quantum confinement in size-selected, surface-oxidized silicon nanocrystals,” *Science*, vol. 262, pp. 1242–1244, 1993.
- [44] Y. He, C. Fan, and S. T. Lee, “Silicon nanostructures for bioapplications,” *Nano Today*, vol. 5, no. 4, pp. 282–295, 2010.
- [45] B.-H. Kim, C.-H. Cho, J.-S. Mun, M.-K. Kwon, T.-Y. Park, J. S. Kim, C. C. Byeon, J. Lee, and S.-J. Park, “Enhancement of the External Quantum Efficiency of a Silicon Quantum Dot Light-Emitting Diode by Localized Surface Plasmons,” *Adv. Mater.*, vol. 20, no. 16, pp. 3100–3104, Aug. 2008.
- [46] B. H. Kim, C. H. Cho, S. J. Park, N. M. Park, and G. Y. Sung, “Ni/Au contact to silicon quantum dot light-emitting diodes for the enhancement of carrier injection and light extraction efficiency,” *Appl. Phys. Lett.*, vol. 89, pp. 11–13, 2006.
- [47] J. D. Holmes, K. J. Ziegler, R. C. Doty, L. E. Pell, K. P. Johnston, and B. A. Korgel, “Highly luminescent silicon nanocrystals with discrete optical transitions,” *J. Am. Chem. Soc.*, vol. 123, no. 10, pp. 3743–3748, 2001.
- [48] M. C. Beard, K. P. Knutsen, P. Yu, J. M. Luther, Q. Song, W. K. Metzger, R. J. Ellingson, and A. J. Nozik, “Multiple exciton generation in colloidal silicon nanocrystals,” *Nano Lett.*, vol. 7, pp. 2506–2512, 2007.
- [49] F. Meillaud, A. Shah, C. Droz, E. Vallat-Sauvain, and C. Miazza, “Efficiency limits for single-junction and tandem solar cells,” *Sol. Energy Mater. Sol. Cells*, vol. 90, pp. 2952–2959, 2006.
- [50] J. Heitmann, F. Müller, M. Zacharias, and U. Gösele, “Silicon nanocrystals: Size matters,” *Adv. Mater.*, vol. 17, no. 7, pp. 795–803, 2005.

- [51] C. M. Hessel, D. Reid, M. G. Panthani, M. R. Rasch, B. W. Goodfellow, J. Wei, H. Fujii, V. Akhavan, and B. A. Korgel, “Synthesis of ligand-stabilized silicon nanocrystals with size-dependent photoluminescence spanning visible to near-infrared wavelengths,” *Chem. Mater.*, vol. 24, pp. 393–401, 2012.
- [52] J. Zou, R. K. Baldwin, K. A. Pettigrew, and S. M. Kauzlarich, “Solution synthesis of ultrastable luminescent siloxane-coated silicon nanoparticles,” *Nano Lett.*, vol. 4, pp. 1181–1186, 2004.
- [53] D. S. English, L. E. Pell, Z. Yu, P. F. Barbara, and B. A. Korgel, “Size Tunable Visible Luminescence from Individual Organic Monolayer Stabilized Silicon Nanocrystal Quantum Dots,” *Nano Lett.*, vol. 2, pp. 681–685, 2002.
- [54] X. Li, Y. He, S. S. Talukdar, and M. T. Swihart, “Process for preparing macroscopic quantities of brightly photoluminescent silicon nanoparticles with emission spanning the visible spectrum,” *Langmuir*, vol. 19, no. 5, pp. 8490–8496, 2003.
- [55] H. Li, M. T. Lusk, R. T. Collins, and Z. Wu, “An Optimal Size Regime for Oxidation Resistant Silicon Quantum Dots An Optimal Size Regime for Oxidation Resistant Silicon Quantum Dots,” *ACS Nano*, vol. 6, no. 11, pp. 9690–9699, 2012.
- [56] Z. Iqbal and S. Veprek, “Raman scattering from hydrogenated microcrystalline and amorphous silicon,” *J. Phys. C Solid State Phys.*, vol. 15, pp. 377–392, 1982.
- [57] G. Viera, S. Huet, and L. Boufendi, “Crystal size and temperature measurements in nanostructured silicon using Raman spectroscopy,” *J. Appl. Phys.*, vol. 90, no. 2001, pp. 4175–4183, 2001.
- [58] M. H. Brodsky, M. Cardona, and J. J. Cuomo, “Infrared and Raman spectra of the silicon-hydrogen bonds in amorphous silicon prepared by glow discharge and sputtering,” *Phys. Rev. B*, vol. 16, no. October 1977, pp. 3556–3571, 1977.
- [59] J. D. Fields, S. McMurray, L. R. Wienkes, J. Trask, C. Anderson, P. L. Miller, B. J. Simonds, J. Kakalios, U. Kortshagen, M. T. Lusk, R. T. Collins, and P. C. Taylor, “Quantum confinement in mixed phase silicon thin films grown by co-deposition plasma processing,” *Sol. Energy Mater. Sol. Cells*, vol. 129, pp. 7–12, 2013.
- [60] H. Richter, Z. P. Wang, and L. Ley, “The one phonon Raman spectrum in microcrystalline silicon,” *Solid State Commun.*, vol. 39, no. 5, pp. 625–629, 1981.
- [61] Z. Ma, X. Liao, G. Kong, and J. Chu, “Absorption spectra of nanocrystalline silicon embedded in SiO₂ matrix,” *Appl. Phys. Lett.*, vol. 75, no. 13, p. 1857, 1999.
- [62] B. Garrido Fernandez, M. López, C. García, A. Pérez-Rodríguez, J. R. Morante, C. Bonafos, M. Carrada, a. Claverie, M. López, C. García, A. Pérez-Rodríguez, J. R. Morante, C. Bonafos, M. Carrada, and a. Claverie, “Influence of average size and

- interface passivation on the spectral emission of Si nanocrystals embedded in SiO₂,” *J. Appl. Phys.*, vol. 91, no. 2002, pp. 798–807, 2002.
- [63] C. Meier, A. Gondorf, S. Lüttjohann, A. Lorke, and H. Wiggers, “Silicon nanoparticles: Absorption, emission, and the nature of the electronic bandgap,” *J. Appl. Phys.*, vol. 101, no. 10, p. 103112, 2007.
- [64] K. Tanaka and A. Nakajima, “Observation of Phonon Structures in Porous Si Luminescence,” *Phys. Rev. Lett.*, vol. 70, no. 23, pp. 3659–3662, 1993.
- [65] P. D. J. Calcott, K. J. Nash, L. T. Canham, M. J. Kane, and D. Brumhead, “Identification of radiative transitions in highly porous silicon,” *J. Phys. Condens. Matter*, vol. 5, pp. L91–L98, 1999.
- [66] J.-W. Luo, P. Stradins, and A. Zunger, “Matrix-embedded silicon quantum dots for photovoltaic applications: a theoretical study of critical factors,” *Energy Environ. Sci.*, vol. 4, p. 2546, 2011.
- [67] M. Wolkin, J. Jorne, P. Fauchet, G. Allan, and C. Delerue, “Electronic States and Luminescence in Porous Silicon Quantum Dots: The Role of Oxygen,” *Phys. Rev. Lett.*, vol. 82, no. August 2015, pp. 197–200, 1999.
- [68] W. Cai and V. M. Shalaev, *Optical Metamaterials: Fundamentals and Applications*. New York: Springer, 2010.
- [69] H. G. Grimmeiss and L. Å. Ledebø, “Spectral distribution of photoionization cross sections by photoconductivity measurements,” *J. Appl. Phys.*, vol. 46, no. 1975, pp. 2155–2162, 1975.

APPENDIX – PERMISSION
AIP PUBLISHING LLC LICENSE
TERMS AND CONDITIONS

Aug 12, 2015

All payments must be made in full to CCC. For payment instructions, please see information listed at the bottom of this form.

License Number	3686290039270
Order Date	Aug 12, 2015
Publisher	AIP Publishing LLC
Publication	Applied Physics Letters
Article Title	Highly efficient charge transfer in nanocrystalline Si:H solar cells
Author	K. G. Kiriluk, J. D. Fields, B. J. Simonds, et al.
Online Publication Date	Apr 1, 2013
Volume number	102
Issue number	13
Type of Use	Thesis/Dissertation
Requestor type	Student
Format	Print and electronic
Portion	Figure/Table
Number of figures/tables	1
Title of your thesis /dissertation	Direct measure of the band edge optical absorption of silicon nanostructures using Photothermal Deflection Spectroscopy
Expected completion date	Sep 2015
Estimated size (number of pages)	70

Total 0.00 USD

Terms and Conditions

AIP Publishing LLC Terms and Conditions: Permissions Uses

AIP Publishing LLC ("AIPP") hereby grants to you the nonexclusive right and license to use and/or distribute the Material according to the use specified in your order, on a onetime basis, for the specified term, with a maximum distribution equal to the number that you have ordered. Any links or other content accompanying the Material are not the subject of this license.

1. You agree to include the following copyright and permission notice with the reproduction of the Material: "Reprinted with permission from [FULL CITATION]. Copyright [PUBLICATION YEAR], AIP Publishing LLC." For an article, the copyright and permission notice must be printed on the first page of the article or book chapter. For photographs, covers, or tables, the copyright and permission notice may appear with the Material, in a footnote, or in the reference list.

2. If you have licensed reuse of a figure, photograph, cover, or table, it is your responsibility to ensure that the material is original to AIPP and does not contain the copyright of another entity, and that the copyright notice of the figure, photograph, cover, or table does not indicate that it was reprinted by AIPP, with permission, from another source. Under no circumstances does AIPP, purport or intend to grant permission to reuse material to which it does not hold copyright.

3. You may not alter or modify the Material in any manner. You may translate the Material into another language only if you have licensed translation rights. You may not use the Material for promotional purposes. AIPP reserves all rights not specifically granted herein.

4. The foregoing license shall not take effect unless and until AIPP or its agent, Copyright Clearance Center, receives the Payment in accordance with Copyright Clearance Center Billing and Payment Terms and Conditions, which are incorporated herein by reference.

5. AIPP or the Copyright Clearance Center may, within two business days of granting this license, revoke the license for any reason whatsoever, with a full refund payable to you. Should you violate the terms of this license at any time, AIPP, AIP Publishing LLC, or Copyright Clearance Center may revoke the license with no refund to you. Notice of such revocation will be made using the contact information provided by you. Failure to receive such notice will not nullify the revocation.

6. AIPP makes no representations or warranties with respect to the Material. You agree to indemnify and hold harmless AIPP, AIP Publishing LLC, and their officers, directors, employees or agents from and against any and all claims arising out of your use of the Material other than as specifically authorized herein.

7. The permission granted herein is personal to you and is not transferable or assignable without the prior written permission of AIPP. This license may not be amended except in a writing signed by the party to be charged.

8. If purchase orders, acknowledgments or check endorsements are issued on any forms containing terms and conditions which are inconsistent with these provisions, such inconsistent terms and conditions shall be of no force and effect. This document, including the CCC Billing and Payment Terms and Conditions, shall be the entire agreement between the parties relating to the subject matter hereof.

This Agreement shall be governed by and construed in accordance with the laws of the State of New York. Both parties hereby submit to the jurisdiction of the courts of New York County for purposes of resolving any disputes that may arise hereunder.

Questions? customercare@copyright.com or +18552393415 (toll free in the US) or +19786462777.